The prion-like characteristic of ORF3 contributes to virion release and pathogenesis of Hepatitis E virus

Yajing Wang[#1], Houlu Tian[#1,2], Na Shi[2], Chunyan Wu[1], Yaowei Huang[3], Yongling Yang[4], Qiang Ding[5], Xu Zheng[1], Qin Zhao[1], Zhaonong Hu[6], Jiaojiao Luo[6], Lele Feng[6], Lingdong Xu[7], Mick F. Tuite[8], Hongying Chen[2,9 *] and Yuchen Nan[1 *]

[1]Department of Preventive Veterinary Medicine, College of Veterinary Medicine, Northwest A&F University, Yangling, 712100, China.

[2]College of Life Sciences, Northwest A&F University, Yangling, Shaanxi, 712100, China.

[3]Guangdong Laboratory for Lingnan Modern Agriculture, College of Veterinary Medicine, South China Agricultural University, Guangzhou, Guangdong, 510642, China

[4]Department of Infectious Diseases, The Affiliated Taizhou People's Hospital of Nanjing Medical University, Taizhou, Jiangsu, 225300, China

[5]Center for Infectious Disease Research, School of Medicine, Tsinghua University, Beijing, China

[6]Institute of Pesticide Science, College of Plant Protection, Northwest A&F University, Yangling, Shaanxi, 712100, China.

[7]Laboratory Animal Center, Zhejiang University, Hangzhou, Zhejiang, China

[8]School of Biosciences, University of Kent, Canterbury, Kent CT2 7NJ, Canterbury, UK

[9] Institute of Future Agriculture, Northwest A&F University, Yangling, Shaanxi, 712100, China.

[#]Co-first author

[*] **Correspondence:** Dr. Yuchen Nan; Department of Preventive Veterinary Medicine, College of Veterinary Medicine, Northwest A&F University, Yangling, 712100, China; Tel: 86- 029-87091117; Fax:86- 029-87091032; Email: nanyuchen2015@nwsuaf.edu.cn;

Dr. Hongying Chen; College of Life Sciences, Northwest A&F University, Yangling, Shaanxi, 712100, China; Tel: 86- 029-87092262; Fax:86-029-87092262; chenhy@nwsuaf.edu.cn

Abstract

Hepatitis E virus (HEV), the causative agent of hepatitis E, is threatening public health globally. Due to the shortage of efficient *in vitro* cell culture systems and *in vivo* model, the viral replication and pathogenesis mechanisms remain largely unknown. Here, we found that HEV-ORF3 protein showed prion-like properties in HEV-infected cells and existed as both monomer and SDS-resistant aggregates forms. In an *in vitro* cell-free model, incubation of ORF3 monomer with its aggregates could effectively convert ORF3 monomer into aggregates, mirroring a typical characteristic of prion. In addition, the prion domain (PrD) of a classic yeast prion Sup35 could be functionally replaced by full length HEV-ORF3 or its N-terminal candidate PrD (cPrD). An F10S substitution in the ORF3-cPrD impaired HEV-ORF3 aggregation propensity and blocked the function of ORF3 in enhancing the stability of microtubules in HEV-infected cells, thus led to the inhibition of viral capsid translocation to microtubules and virion release from infected cells. In Mongolian gerbils models, HEV bearing ORF3F10S mutation demonstrated attenuated virulence *in vivo* compared with wild-type HEV, as evidenced by reduced viremia and viral shedding, as well as alleviated pathological changes of liver tissue in gerbils infected by HEV-ORF3F10S mutant. In conclusion, our data suggest that HEV-ORF3 is a novel prion-like protein which is involved in viral capsid translocation and virion release, supporting the hypothesis that the self-propagating properties of prion proteins or prion-like proteins are widely exploited in nature and play diverse roles in physiological function.

Keyword: Hepatitis E virus (HEV), ORF3, Prion, capsid transport, virus release, microtubule,

Significance

Prions and prion-like proteins can form self-propagating protein aggregates which has been identified in animals, plants and diverse microorganisms. Here, we demonstrate HEV-ORF3 forms self-propagating aggregates similar to prions, which is the first prion-like protein to be experimentally defined from mammalian RNA virus. Importantly, the prion-forming propensity of HEV-ORF3 is involved in the stabilization of cytoskeleton, promoting translocation of viral capsid to microtubules thus facilitating the release of virus particles, and therefore also contributes to the pathogenesis of HEV *in vivo*. HEV-ORF3 is a novel example of functional prion-like protein which employs the self-sustaining conformational state in its normal physiological function.

Introduction

Hepatitis E virus (HEV) is a quasi-enveloped, single-stranded positive-sense RNA virus. It is categorized within an expanding family of *Hepeviridae* (1), contains several zoonotic, anthropotropic and animal-restricted HEV species and HEV-like viral isolates (2). HEV infection was originally thought to be solely restricted to humans. However, the discovery of HEV in swine in 1997 suggests HEV has wider host range and is actually zoonotic (3). Moreover, chronic HEV infection, HEV-related acute hepatic failure, and HEV-caused extrahepatic manifestations have been frequently reported in recent years (4), suggesting a complicated mechanism underlying HEV-related diseases.

HEV contains a 7.2 kb mRNA-like genome, which is capped and polyadenylated (2). To date, three well-recognized open reading frames (ORFs) have been identified regardless HEV genotypes or species (2), while the presence of an additional ORF4 is only identified in HEV-1 (5). The HEV-ORF1 protein is translated directly from the viral genome which acts as the viral replicase (6), whereas ORF2 and ORF3 are partially or completely overlapped and translated from sub-genomic RNA (7). HEV-ORF2 encodes the major capsid protein (8). HEV-ORF3 encodes a 114-aa protein (7, 9), which carries two hydrophobic domains within its N-terminal half and two proline-rich domains within its C-terminal portion (10, 11), along with a MAP kinase phosphorylation site (12). Although not required for viral RNA replication *in vitro* , HEV-ORF3 protein is essential for HEV virion release from infected cells and indispensable for HEV infection *in vivo* (9, 13). Studies have shown that a PSAP motif is required for the formation of membrane-associated HEV particles, a process that relies on the association of ORF3 protein with lipids (14). Besides, HEV-ORF3 forms an ion channel that shares key structural features with class I viroporins, contributes to virus particle release (8).

In our experiment on ORF3 overexpression (Fig. S1A), we observed that ORF3 from HEV-1 Sar55 strain expressed in HEK-293T cells was able to form

high-molecular-weight aggregates, which mirrors the characteristics of LEF10, the first virus-encoded prion-like protein identified from member of *Baculoviridae* (15). Prions are self-propagating protein that were originally associated with neurodegenerative diseases in mammals. In recent years, emerging discoveries of prion-like proteins in plants, cellular microbes and acellular microorganisms indicate that proteins bearing prions-like behavior are neither exclusive to mammalian host nor necessarily pathogenic. These prion-like proteins are structurally and functionally diverse, which act as epigenetic information carriers and have important regulatory functions (16, 17).

In this study, by employing cell-free *in vitro* assay and well-characterized yeast reporter system, we demonstrate that HEV-ORF3 behaves like prion and bears a prion domain (PrD) which can functionally replace the PrD of Sup35, a well-characterized yeast prion. Furthermore, by generating ORF3 mutant with reduced aggregation property, the role of the prion-like property of ORF3 in HEV infection was investigated both *in vitro* and *in vivo*.

Results

The HEV-ORF3 protein behaves like a prion

In our previous studies, we observed that ORF3 formed SDS-resistant, high-molecular-weight aggregates when transiently overexpressed in different cell lines (HEK-293T, S10-3) (Fig. S1A). Since a recent report indicated that ORF3 could be secreted from cells (18), the secreted ORF3 (sORF3) was enriched and compared with intracellular ORF3 from overexpressed HEK-293T cells. The data showed that sORF3 did not form aggregates as intracellular ORF3, suggesting that the overexpressed HEV-ORF3 existed as two forms: monomer and SDS-resistant aggregates (Fig. S1B). To investigate if the SDS-resistant ORF3 aggregates existed in HEV-infected cells. a cell-adapted HEV-3 KernowC1-p6 *in vitro* culture system and an HEV-3 KernowC1-p6 ORF3 specific Mab were employed to examine ORF3 natively expressed in HEV-replicating cells. As shown in Fig. 1A, after transfection of S10-3 cells with *in vitro* transcribed HEV-RNAs of wild-type HEV(HEV-WT) and ORF3 deletion mutant (HEVΔORF3), SDS-resistant aggregates of the ORF3 protein were only detected in HEV-WT RNA transfected cells, but not in HEVΔORF3 RNA transfected cells or enriched sORF3. Using semi-denaturing detergent agarose gel electrophoresis (SDD-AGE), a common assay for the detection of amyloid-forming proteins (19), intracellular ORF3 was detected as diffuse bands while only a low molecular weight band was detected for sORF3, further confirming the formation of aggregates by intracellular ORF3. In HepG2/C3A cells stably infected with HEV-WT, similar aggregates were detected (Fig. 1B).

To confirm ORF3's aggregation was a consequence of self-assembly rather than covalently attached to substrate like ubiquitin, a bimolecular fluorescence complementation (BiFC) assay was conducted. Strong florescence was observed only in cells expressing N-terminal Venus fused ORF3 (VN173-ORF3) and C-terminal Venus fused ORF3 (VC155-ORF3), confirming the self-aggregation of the ORF3 (Fig. S1C). Consistent with the BiFC result, aggregates of VN173-ORF3 were observed in SDS-PAGE and SDD-AGE by multiple antibodies (Fig. S1D).

To further investigate the prion-like characteristics of HEV-ORF3, negative-stained Transmission Electron Microscopy (TEM) and Congo Red (CR) Stain were used to observe ORF3 enriched from HEV-infected S10-3 cells by immune precipitation (IP) using ORF3-specific Mab. The ORF3 protein enriched from HEV-infected S10-3 cells formed fibril-like structure under TEM and exhibited apple-green birefringence under polarized light after CR stain (Fig. 1C), an dye for detecting amyloid's fiber-like structure (20). The ORF3 protein enriched from ORF3-overexpressing HEK-293T cells showed similar properties (Fig. 1D). Since HEV-ORF3 is known to associate with microtubules (10, 12, 18), we examined whether the enriched ORF3 was contaminated by microtubule filaments. Consistent with a previous report (12), microtubules were not co-precipitated with ORF3 by anti-ORF3 antibody in Co-IP assay (Fig. S2A), while association between ORF3 and microtubule was observed by fluorescence microscopy. Such discrepancy may be caused by technical limitation of Co-IP. Conversely, microtubules extracted from S10-3 cells showed a rod-like structure under TEM (Fig. S2B), which was clearly

different from the fiber-like structure of ORF3 aggregates. Meanwhile, sORF3 monomers showed no fiber-like structure under TEM (Fig. S2C). Collectively, these data suggested that intracellular HEV-ORF3 formed fibril-like structure and demonstrated prion-like characteristics.

As another mammalian prion-like protein, Mitochondrial Antiviral Signaling Protein (MAVS) demonstrated a HSP90 dependent assembly of prion-like aggregates (21), HSP90 inhibitor Geldanamycin was employed to treat ORF3-expressing HEK-293T cells and reduced ORF3 aggregates were observed (Fig. 1E), suggesting a similar role played by HSP90 during ORF3 aggregation. Additionally, since prion-form of MAVS can efficiently convert MAVS monomer into prion-like aggregates (21), the IP enriched sORF3 monomer with MYC-tag was incubated with the whole cell lysate of HEK-293T cells containing untagged ORF3 aggregates. As demonstrated in Fig. 1F, the MYC-tagged ORF3 monomer was effectively converted into aggregates form by pre-existing ORF3 aggregates, representing a typical property resembling the infectious conformations of mammalian prion and prion-like proteins such as MAVS (19, 21).

To further verify the prion-like behavior of HEV-ORF3, a yeast prion reporter system based on the well-characterized [PSI^{+}] prion phenotype of the *Saccharomyces cerevisiae* translation termination factor Sup35 was utilized. In this reporter system, when the N-terminal prion-forming domain (PrD) of Sup35 is replaced by other PrD bearing protein, it will endow yeast cells with a [PSI^{+}]-like phenotype (22). Here, the PrD of Sup35 was substituted by HEV-ORF3 to generate a ORF3-Sup35MC fusion

protein. Like the [*PSI*$^{+}$] phenotype caused by the prion form of Sup35, the yeast strain harboring the ORF3-Sup35MC protein exhibited both [*ORF3*$^{+}$] and [*orf3*$^{-}$] phenotypes (Fig. 2A) (yeast strains and plasmids for Sup35 proteins expression, see Table S1). SDD-AGE confirmed that the ORF3-Sup35MC formed aggregates in [*ORF3*$^{+}$] cells, whereas only monomer could be detected in [*orf3*$^{-}$] cells (Fig. 2B).

In the yeast where Sup35 or ORF3-Sup35MC was soluble, protein synthesis is efficiently terminated at the premature UGA in the yeast *ade1-14* allele, which results in red colonies on the 1/4 YPD plate and a failure to grow on SD-Ade medium (23). By contrast, when the cells carry prion-like aggregates of ORF3-Sup35MC, they give rise to white colonies on both the 1/4 YPD plate and growth on SD-Ade medium due to the read-through of the UGA (23). Hsp104 is a chaperone required for the heritability of [*PSI*$^{+}$] and other yeast prions (23). Therefore, an Hsp104-specific inhibitor guanidine hydrochloride (GdnHCl) was applied to inactivate Hsp104 (24). By growing [*ORF3*$^{+}$] yeast on rich medium containing 5 mM GdnHCl, the [*ORF3*$^{+}$] was lost resulting in [*orf3*$^{-}$] cells as is observed with [*PSI*$^{+}$] cells (Fig. 2C). Further data indicated that the deletion of the *HSP104* gene eliminated the [*ORF3*$^{+}$] phenotypes (Fig. 2D and 2E), indicating that the [*ORF3*$^{+}$] phenotype requires functional Hsp104 for the *de novo* induction and propagation. Since Hsp104-dependent characteristics have been observed for almost all identified yeast prions (23), it further demonstrates that the [*ORF3*$^{+}$] phenotype was not caused by non-epigenetic effects but by the *bona fide* prion property of the ORF3 protein. Moreover, by counting the red and white colonies on three 1/4 YPD plates from three

196 independent plasmid transformation and shuffling experiments, 89.98% of the yeast
197 cells expressing ORF3-Sup35MC formed [*orf3*$^{-}$] colonies, and 10.02% formed
198 [*ORF3*$^{+}$] colonies (Table S2). During the propagation of [*ORF3*$^{+}$] and [*orf3*$^{-}$] colonies,
199 the white or red phenotype was stable through multiple generations although the
200 switch of phenotype (0.89% from white to red, 1.81% from red to white) could be
201 observed at a very low frequency (Table S2). As the ORF3-Sup35MC fusion protein
202 was controlled by the *SUP35* gene promoter, it indicated that the prion-like
203 conformation of ORF3 was self-perpetuating and the low expression level was
204 sufficient to maintain its prion-like state. Although a recent report suggests that the
205 yeast system alone cannot address specific aspects of amyloidosis seen in humans
206 (25), by showing self-perpetuating ORF3 aggregates could efficiently convert ORF3
207 monomer into functional aggregates in a self-catalytic manner *in vitro*, our data
208 indicated that HEV-ORF3 demonstrates prion-like behavior.

209 **The N-terminal half of HEV-ORF3 acts as prion-forming domain**

210 Most prion-like proteins identified so far have glutamine/asparagine (Q/N)-rich
211 PrD, which is not presented in the HEV-ORF3. Using bioinformatics tools to search
212 for potential PrD from ORF3 (26), we did not identify a distinct candidate PrD (cPrD)
213 by PLAAC (Fig. S3A), but found several short amyloidogenic regions in the
214 N-terminal part of ORF3 protein by AGGRESCAN and FoldAmyloid (Fig. S3B and
215 S3C). Therefore, HEV-ORF3 was truncated for identifying cPrD (Fig. 3A). Deletion
216 of the N terminal 25aa of ORF3 ($ORF3_{T2}$) completely abolished the formation of
217 aggregates (Fig. 3B), while $ORF3_{T1}$ alone was able to form aggregates. The $ORF3_{T3}$

bearing the N-terminal 1 to 60 aa of ORF3 formed aggregates similar to the full length ORF3 in SDD-AGE. These results demonstrate that the N-terminal region endowed on ORF3 the ability to form aggregates.

When the Sup35 PrD was replaced by ORF3 truncations, the yeast cells expressing $ORF3_{T1}$-Sup35MC and $ORF3_{T3}$-Sup35MC formed white or light brown colonies like [PSI^{+}] yeast, whereas the cells expressing $ORF3_{T2}$-Sup35MC and $ORF3_{T4}$-Sup35MC were red, close to the color of the colonies harboring $Sup35N_{1\text{-}5}$MC (Fig. S3D). Further analysis revealed that $ORF3_{T1}$-Sup35MC only formed white colonies (Fig. S3E), suggested that $ORF3_{T1}$-Sup35MC protein probably only existed as aggregates. However, the yeast strain harboring the recombinant $ORF3_{T3}$-Sup35MC protein exhibited both [$ORF3^{+}$] and [$orf3^{-}$] like phenotypes (Fig. 3C and 3D), suggesting that the full cPrD of HEV-ORF3 was located in the 1-60 aa region. Moreover, by propagation of [$ORF3_{T3}^{+}$] and [$orf3_{t3}^{-}$] colonies on 1/4 YPD plate, we found that the white phenotype was more stable than the red phenotype, with the switch frequency was about 3.88% from red to white colonies and about 0.51% from white to red colonies (Fig. 3D and Table S3). On SD-Ade medium, [$ORF3_{T3}^{+}$] cells grew normally, but [$orf3_{t3}^{-}$] cells stopped growing due to the efficient translation termination by soluble Sup35 at the *ade1-14* premature stop codon (Fig. 3E). These data suggested that $ORF3_{T3}$ harboring the first three amyloidogenic regions acted as the functional cPrD and the first 25 aa contributed to ORF3 aggregation.

Previous investigation found that the ORF3 N-terminus was essential for the formation of microtubule-like filaments, but the fusion protein only containing the

N-terminal 25 aa of ORF3 formed aggregated dots in the cells (10). Consistent with these observation, $ORF3_{T1}$-GFP and $ORF3_{T3}$-GFP produced larger (Fig. 3F) and more number of punctate aggregates than ORF3-GFP in yeast cells (Fig. 3F and 3G), whereas $ORF3_{T2}$-GFP and $ORF3_{T4}$-GFP were evenly distributed. SDD-AGE analysis of these yeast strains further confirmed the aggregation status of $ORF3_{T1}$-GFP and $ORF3_{T3}$-GFP (Fig. 3H).

Since prion-like protein has never been identified from RNA viruses, to understand biological significance of the prion-forming character of HEV-ORF3, we sought to generate PrD-domain/function impaired ORF3 mutant. First, continuous triple-alanine mutation was introduced into aa 2 to 25 for generating a set of 8 ORF3 mutants (M1 to M8, corresponding to the replacement of original aa 2-4 until 23-25 of ORF3 with triple alanine). These mutants demonstrated variable ability to form aggregates (Fig. 4A), but M3 harboring mutations at positions 8-10 showed the lowest aggregation. In yeast, quantification of florescence punctate aggregates from different yeast strains suggested that the $ORF3^{M3}$-GFP mutant exhibited decreased aggregation tendency (Fig. 4B). Expression of the $ORF3^{M3}$-Sup35MC protein generated yeast cells with a weak Ade^{+} phenotype closer to that observed for [*psi*$^{-}$] cells on 1/4 YPD plate (Fig. 4C), as the cells having $ORF3^{M3}$-Sup35MC formed fewer white colonies than the cells expressing ORF3-Sup35MC and its other mutants (Table S4).

To further pin down the key amino acid residue (s), single alanine residue was introduced at positions 8, 9 or 10 of ORF3, and the aggregation abilities of the mutants were compared. Although the ORF3F10A mutant only resulted in a slight

reduction of aggregates in SDS-PAGE, it produced the least amount of aggregates as defined by SDD-AGE (Fig. S4), suggesting that the phenylalanine at position 10 (F10) was a key amino acid involved in the prion-like behavior. However, as HEV-ORF2 and ORF3 are partially overlapped, the F10A mutation in ORF3 will cause a non-synonymous amino acid change in ORF2. Therefore, we substituted the hydrophobic F10 with three different hydrophilic amino acids (serine, tyrosine and cysteine) as this would not introduce aa change in ORF2. The F10S mutant showed a dramatically reduced ability to form aggregates (Fig. 4D). By contrast, when the MYC-tagged ORF3F10S monomer was enriched and then incubated with the whole cell lysate of HEK-293T cell expressing ORF3WT, the aggregates converted from ORF3F10S monomer were significantly reduced (Fig. 4E), further suggesting that F10S mutation impaired the prion-like aggregation of ORF3. Meanwhile, the F10S mutation also resulted in fewer white colonies (3.05%) than the wild type ORF3 in yeast (10.02%) (Table S4 and Fig. S5A), and yeast expressing ORF3^{F10S} mutant had a reddish phenotype on 1/4 YPD medium and impaired growth ability on SD-Ade medium compared with the cells expressing ORF3WT (Fig. 4F). SDD-AGE analysis also detected a reduced aggregation ability of ORF3^{F10S}-Sup35MC in yeast cells (Fig. 4G). During the propagation of [*ORF3*$^{F10S+}$] and [*orf3*$^{F10S-}$] colonies, the white phenotype of the F10S mutant was less stable than wild type ORF3 (8.85% *vs* 0.89% colonies switched from white to red colour) (Table S4 and Fig. S5A), although [*ORF3*$^{F10S+}$] also formed SDS-resistant polymers like [*ORF3*$^{+}$] (Fig. S5B). Furthermore, ORF3WT and ORF3F10S were enriched and subjected to EM and CR

staining. As showed in Fig. S6, the ORF3F10S lost the ability to form fibril-like structure and showed no apple-green birefringence in CR staining assay. These data demonstrate that the F10S mutation in the cPrD domain significantly reduced the capacity of HEV-ORF3 to form prion-like aggregates.

Mutation of the ORF3 prion-forming domain prevents virus release from HEV-infected cells

To investigate the role of the ORF3 prion-forming function in the HEV replication, mutagenesis assay was carried out to generate an HEV infectious clone harboring the ORF3F10S mutation. Similar to the wild type virus, the HEV-3 KernowC1-p6 ORF3^{F10S} virus was viable as both ORF2 and ORF3 proteins were detectable after RNA transfection (Fig. 5A). Using SDS-PAGE and SDD-AGE, a reduction of ORF3 aggregation was observed in the cells transfected with HEV-3 KernowC1-p6 ORF3^{F10S} (Fig. 5B), but ORF2 protein was obviously higher than cells transfected with the WT RNA. By RT-qPCR, it was revealed that the positive-stranded (+) and negative-stranded (-) HEV-RNA levels were similar among the three groups (Fig. 5C), suggesting that the F10S mutation did not impair HEV-RNA replication. However, the HEV-RNA (+) released into the supernatant was significantly decreased in the ORF3F10S group at 4 and 6 days post transfection and comparable to ORF3 deletion mutant (Fig. 5D).Titration of the released infectious virus particles at 7 days post transfection detected a significant lower virus titer for the F10S mutant than the WT (Fig. 5E), suggesting a strong inhibition of virion release by the introduction of F10S mutation. This might account for the higher intracellular

ORF2 protein level observed in ORF3F10S mutant virus-infected cells (Fig. 5B).

As recent reports indicated that both ORF2 and ORF3 proteins could be directly secreted from HEV infected cells (18, 27), sandwich ELISA assays were conducted to evaluate the secretion of HEV-ORF2/3 in supernatants. While no significant difference of ORF2 secretion was observed among the different groups (Fig. 5F), an enhanced ORF3 secretion was detected in the F10S group (Figure 5G). To further explore whether other potential mutation sites were involved in the prion-like aggregation of ORF3 and virion release, seven ORF3 mutants were generated for evaluating using SDS-PAGE and SDD-AGE, with each mutant containing a single aa mutation in the first 25 aa of ORF3 but caused no change for overlapped ORF2. The ORF3L7Q mutant was shown to have impaired aggregation capacity (Fig. S7), then introduced into infectious clone for rescuing virus (Fig. S8A). Similar to ORF3F10S mutant, a reduction of ORF3 aggregation (Fig. S8B), accumulation of intracellular ORF2 protein (Fig. S8B) and reduction of virion release were observed for HEV-3 KernowC1-p6 ORF3^{L7Q} (Fig. S8D and S8E), whereas the intracellular HEV-RNAs and secreted ORF2 levels were not affected (Fig. S8C and S8F). Meanwhile, an enhanced ORF3 secretion was detected for HEV-3 KernowC1-p6 ORF3^{L7Q} as well (Fig. S8G). Collectively, these data demonstrated that the reduced ORF3 aggregation caused by the mutations in ORF3 prion-forming domain did not influence HEV replication and but obstructed the release of assembled HEV particles.

Mutation in the ORF3 prion-forming domain reduces microtubule stability and the association of ORF2 with microtubule

328 It has been reported that a conserved PSAP motif of HEV-ORF3 is important for
329 its interaction with tumor susceptibility gene 101 (TSG101) (14), a key component of
330 the endosomal sorting complex required for transport (ESCRT) which is involved in
331 budding and biogenesis of quasi-enveloped HEV particles (28, 29). Meanwhile,
332 palmitoylation on the N-terminal cysteine residues of HEV-ORF3 is also required for
333 the HEV release (30). However, the ORF3F10S mutant had a similar binding ability
334 to TSG101 as the wild-type ORF3 (Fig. S9A). Moreover, by employing a acyl-biotin
335 exchange protocol for ORF3 palmitoylation (31), normalization of the amount of
336 palmitoylated ORF3 with the total ORF3 showed that the F10S mutation even caused
337 slightly elevation of palmitoylated ORF3 (Fig. S9B).

338 Besides ESCRT and ORF3 palmitoylation, a previous report demonstrated that
339 enhanced acetylation of tubulin in influenza A virus (IAV)-infected epithelial cells
340 was correlated with increased virion release, whereas depolymerization/deacetylation
341 of tubulin inhibited IAV virion release (32). As HEV-ORF3 expressed in hepatoma
342 cells is associated with microtubules and induces tubulin acetylation, a
343 well-established marker of microtubule stability (10), the subcellular localization and
344 tubulin acetylation level of Venus-tagged ORF3^{F10S} mutant were investigated.
345 Consistent with the previous report(10), wild-type ORF3 showed a filamentous
346 pattern of distribution associated with microtubule, whereas Venus-tagged ORF3^{F10S}
347 abolished the filamentous structure (Fig. 6A). Meanwhile, in microtubule extraction
348 assay, wild-type ORF3 was undetectable in the supernatant, but exclusively detected
349 in the extracted microtubule (pellet part) with increased tubulin acetylation (Fig. 6B).

In comparison, the F10S mutation caused a reduced ORF3 level in the pellet, a slight reduction of tubulin acetylation, and the release of the ORF3 in the supernatant (Fig. 6B), suggesting that the F10S mutation reduced the association of ORF3 with microtubule.

Microtubules undergo dynamic changes of assembly and disassembly. To figure out if the enhanced microtubule stability was associated with the prion-like characteristics of HEV-ORF3, the microtubule stabilizer Paclitaxel and assembly inhibitor Indibulin were used. It revealed that wild-type ORF3 conferred resistance to a low dose (1μM) Indibulin treatment, whereas the F10S mutant lost the ability (Fig. 6C). The Indibulin has been proven to dampen microtubule dynamics by perturbing the localization of EB1 at the growing microtubule ends (33). This antagonistic effect of ORF3 to Indibulin indicates that prion-like aggregation of ORF3 is required for its microtubules association and the associated ORF3 aggregates probably enhance the stability of microtubules by promoting their assembly.

HEV-ORF3 has been reported to be a functional ion channel protein required for the release of HEV particles (8). To investigate if the F10S mutation affects the ion channel function of ORF3 in facilitating ion fluxes across the plasma membrane, an ion channel assay was conducted in *X. laevis* oocytes using two-electrode voltage-clamp procedure (8). The voltage protocol to determine the instantaneous current–voltage relations and representative current traces recorded for oocytes (ORF3WT mRNA-injected, ORF3F10S mRNA-injected and MOCK) were presented in Fig. S10A and S10B, respectively. A similar current–voltage relationship was

observed between the oocytes expressing ORF3WT and ORF3F10S (Fig. 6D), and the expression of ORF3WT and ORF3F10S on the outer oocyte membrane was confirmed by immunofluorescence (Fig. 6E), therefore the influence of the F10S mutation on the ion channel activity of ORF3 was ruled out.

Similar to ORF3 overexpressing cells, enhanced tubulin acetylation was observed in S10-3 cells transfected with WT HEV-RNA (1.75 VS 1, compared to MOCK transfected cells), whereas the acetylated tubulin level was much lower in cells transfected with Kernowc1-p6-ORF3^{F10S} mutant (0.94 VS 1.75, compared to HEV-WT) (Fig. 7A, and data quantification results from three independent experiments are shown in Fig. 7B). When S10-3 cells stably infected with HEV were treated with non-cytotoxic dose (below 1μM) of Nocodazole, the drug treatment impaired the release of HEV (Fig. 7C) and consequently caused the intracellular accumulation of HEV-ORF2 (Fig. 7D). Similar to ORF3-overexpressing cells, extraction of microtubule from HEV-infected S10-3 cells showed that the ORF3 was exclusively detected in the pellet with increased tubulin acetylation (Fig. 7E), whereas the F10S mutation resulted in the release of a portion of ORF3 protein in the supernatant with a slight reduction of tubulin acetylation. As ORF3 protein interacts with the non-glycosylated form of ORF2 (34), the major component of infectious particles (35), existence of ORF2 in different portion of microtubule extraction was examined. It is notable that ORF2 protein was only detected in the pellet association with microtubule in HEV-WT infected cells (Fig. 7E), while abundant ORF2 protein was detected in the supernatant free of tubulin in F10S mutant virus infected cells,

suggesting that the ORF3F10S mutation blocked association of ORF2 with microtubule. Therefore, these data indicated that HEV-ORF3's prion-like aggregation stabilizes host microtubules for the microtubule-associated transport of ORF2, thus facilitates the HEV virion release from infected cells.

Impaired prion aggregation of HEV-ORF3 leads to reduced HEV virulence *in vivo*

Mongolian gerbil, the only available model can be infected by HEV-3 KernowC1-p6 (36), was employed to explore the *in vivo* role of HEV-ORF3's prion-like aggregation. Each gerbil was inoculated with wild type HEV (WT) or ORF3^{F10S} mutant virus at a dose of 1×10^9 genome copies. After inoculation, a significant difference of viremia between the two groups was observed at 1 week post infection. Gerbils in HEV-WT group produced much higher levels of viral RNA than ORF3^{F10S} group at 7 dpi (Fig. 8A). As HEVs are largely shed through feces, HEV-RNA in fecal samples were examined and the results showed that animals infected by HEV-WT shed more viruses than those infected by the ORF3^{F10S} mutant virus at 7 and 14 dpi, but shedding of virus dropped to similar level after 3 weeks (Fig. 8B). Meanwhile, a delayed serum conversion for ORF2 antibodies in gerbils infected by the ORF3^{F10S} mutant virus was observed. Compared with the serum conversion in all gerbils of HEV-WT group at 21 dpi, only one gerbil was positive at 28 dpi and two out of five were positive at 35 and 42 dpi in the ORF3^{F10S} group (Fig. 8C).

As liver is the primary target for HEV, livers were taken from infected gerbils at 2 weeks post infection and subjected to histological examination. Consistent with

previously report (36), vacuolation and infiltration of lymphocytic inflammatory cell, as well as focal spotty necrosis was observed in some hepatocytes in HEV-WT infected gerbils (Fig. 8D). In comparison, the pathological changes were milder and immunohistochemistry staining of sections detected a much lower level of HEV antigens in the F10S group (Fig. 8D), suggesting a reduced *in vivo* virulence of HEV-ORF3^{F10S} mutant virus. Quantification of liver disease score for sections of different gerbils groups demonstrated a significant difference between HEV-WT group and F10S group as well (Fig. 8E). In CR staining, the apple-green birefringence could be easily observed in the WT group but was not detected in the F10S group (Fig. S11). It is worth noting that the red staining regions under normal light were close to but not overlayed with the refringence signals under polarized light, probably due to the small amount of ORF3 amyloid present in tissue samples. Such discrepancy during CR stain was also reported for other amyloid proteins (37-39). Although it is suggested that CR staining has some limitations in the detection of amyloidosis in liver (40), combined with *in vitro* data, these *in vivo* results demonstrated that the prion-like aggregation of ORF3 was impaired by introducing F10S mutation *in vivo*, while F10S mutation of the ORF3 PrD also reduces the HEV virulence *in vivo*.

Discussion

Prion, originally defined as a portmanteau of pro (teinaceous) and in (fectious particle) (41), are self-propagating, transmissible protein particles. Prion-forming proteins can fold into multiple conformations and were initially discovered to be associated with neurodegenerative diseases in mammals (42). However, the discovery of prions in the *Saccharomyces cerevisiae* and other microorganisms expanded the scope of the prion concept, and it is now accepted that prion is neither exclusive to mammals nor necessarily associated with disease. So far, prion-forming proteins have not only been identified in various cellular organisms including animal, plant (16), fungi (43) and bacteria (17, 44), but also been discovered in a DNA virus (15). Meanwhile, thousands of prion-like domains have been predicted by bioinformatic methods to be harbored in bacteriophages and eukaryotic viruses (45, 46). In this study, we present that the HEV-ORF3 protein can form prion-like aggregates in mammalian cells, whereas self-perpetuating ORF3 aggregates could efficiently convert ORF3 monomer into aggregates form in a self-catalytic manner. Moreover, ORF3 is able to replace the PrD of Sup35, a classical yeast prion, to display a [PSI^{+}]-like phenotype in yeast. These features support that HEV-ORF3 is the first prion-like protein identified from RNA virus to be experimentally defined.

Similar to baculovirus LEF-10 protein, the HEV-ORF3 protein has no Q/N-rich region, which is used as the principle criteria for the prediction of potential prion-like candidates by algorithms such as PLAAC (26). Nevertheless, the first discovered prion protein, human PrP, does not contain typical Q/N-rich regions. Other yeast

455 prion-forming proteins linked to the [*ISP*$^{+}$], [*MOD*$^{+}$], [*GAR*$^{+}$], [*ESI*$^{+}$] and [*BIG*$^{+}$]
456 phenotypes are also atypical in this context (47). These atypical prions are poorly
457 conserved in their aa sequence, but commonly contain intrinsically disordered regions
458 (IDRs) which serve as PrDs to endow prion-like behavior. The PrDs are often
459 structurally independent and separable from the other regions in prion proteins. Here,
460 our data demonstrate that the non-Q/N-rich ORF3 protein and its cPrD can replace the
461 typical Q/N-rich PrD of Sup35 to nucleate the conversion of Sup35 from a soluble
462 monomer into aggregates and to confer it prion behavior thus supporting their role in
463 prion conformational switching. Moreover, in *in vitro* model, existed ORF3
464 aggregates could convert isolated ORF3 monomer into aggregated forms as well.

465 Prion-like proteins identified from non-mammalian host play important roles in a
466 variety of cellular processes and confer various evolutionary advantages by forming
467 self-propagating aggregates. In most cases, conversion of a protein into its inheritable
468 prion form is associated with amyloid formation and believed to lead to alternation of
469 protein function. For example, a self-sustaining prion-like state of neuronal
470 cytoplasmic polyadenylation element binding protein (CPEB) can be regulated by
471 physiological signals and exploited for long-lasting memory in Drosophila (48).
472 Microbial amyloids have been discovered to play important roles in surface-tension
473 modulation, biofilm stabilization and adhesion (49, 50). Here, by mutagenesis assay,
474 we found that reduction of the prion-forming propensity of HEV-ORF3^{F10S} disturbed
475 its formation of filament-like structure, thereby weakening its ability to stabilize and
476 harness host microtubules for microtubule-dependent transport of HEV-ORF2, which

is required for virion release during HEV replication. Since HEV-ORF2 and ORF3 were overlapped with each other, the potential sites for introducing ORF3 mutant but not bringing mutation to ORF2 were limited. Besides F10S mutant, we also screened for other suitable sites (G2, S3, A6, L7) in the first 25aa of ORF3 for not introducing mutation of ORF2. Our data demonstrated that ORF3L7Q mutation also resulted reduction of virion release as a consequence of reduced ORF3 aggregation. Although not all these mutants were tested for their affection in HEV release, these data from L7Q mutant could strength our claim that ORF3's prion-like aggregation was involved in the release of HEV virion.

Many viruses are known to utilize microtubules for progeny virus transport from replication factory to cell surface for virus release (51, 52). Meanwhile, transportation of viral component via microtubules is essential for some viruses' assembly and egress (53-55), as such transportation process could be blocked by disrupting microtubules (53, 54). It is reported that microtubule plays essential roles in viral nucleocapsid intracellular translocation and assembly for Influenza A virus (56), VSV and Hepatitis B virus (57, 58), and enhanced microtubule stability has been found to be correlated with increased release of infectious influenza virus particles from infected cells (32). Here, in microtubule extraction assay, we found that wild-type ORF3 protein could only be detected in the pellet fraction containing microtubule while ORF3F10S was detected in both the pellet and supernatant fractions, demonstrating that F10S mutation not only reduced the prion-forming propensity of ORF3 but also impaired its microtubule association. Moreover, the

association of ORF3 with microtubule promoted microtubule stability similar to that of paclitaxel, as evidenced by increased tubulin acetylation and resistance to the Indibulin-induced microtubule disassembly.

ORF3 protein is known to interact with the non-glycosylated form of ORF2 protein (34), which is a major component of infectious HEV particles (35). A recent study also demonstrates that palmitoylated ORF3 binds to Annexin II and mutation of the palmitoylation sites in ORF3 disrupts its association with ANXA2, leading to dissociation between ORF3 and the cytoskeleton, therefore blocks the release of HEV particles (18). Consistent with these observations, our data suggest that HEV-ORF3's prion-like aggregation stabilizes host microtubules for the microtubule-dependent transport of non-glycosylated ORF2, thus facilitates the virion release. Meanwhile, since expression of HEV-ORF3 alone is capable to drive the secretion of ORF3 and F10S mutation did not block its secretion, these data suggest that prion-like aggregation and ORF3 palmitoylation are probably involved in different steps but play synergic roles during virion release. In line with its reduced ability to release progeny virus *in vitro*, HEV-3 ORF3^{F10S} mutant demonstrated reduced virulence *in vivo*, as evidenced by lower viremia, delayed serum conversion, and alleviated pathological changes of liver in Gerbils model. These observations suggest that forming of prion-like aggregates is important for HEV-ORF3 to serve its normal function in HEV pathogenesis.

In conclusion, we have discovered the first RNA virus-encoded prion-like protein, HEV-ORF3 and furthermore have demonstrated that the prion-like

aggregation of the HEV-ORF3 protein is required to enhance microtubule stability in HEV-infected cells and then promote HEV virion release, which contributes to HEV infection in animal model. Our data also support the hypothesis that the beneficial forms of prions or prion-like proteins could be functionally diverse and widespread in nature.

Material and Methods

Cells and virus

S10-3 cells, HepG2/C3A cell, HEK-293T cells and HeLa cells were maintained in Dulbecco's Modified Eagle Medium (DMEM; Thermo Fisher Scientific, Waltham, MA, United States) supplemented with 10% FBS (Thermo Fisher Scientific). Full-length RNAs from HEV-3 KernowC1 p6 strain (GenBank: HQ709170.1) and other HEV mutants were obtained by *in vitro* transcription. Details for the rest experiments are presented in the Supporting Information.

Acknowledgement

Funding: This work was supported by grants from the National Natural Science Foundation of China (Grant No. 31672534) and Natural Science Basic Research Plan in Shaanxi Province of China (Grant No. 2024JC-JCQN-24) awarded to Y.N., and a grant from Northwest A&F University awarded to H.C. (Grant No. Z10202190601).

Author contributions: Y.N. and H.C. conceived the project, designed the research and supervised the experiments. Y.W., C.W., X.Z., L. X. and Q.Z. performed the mammalian cells and animal related experiments. H.T. and N.S. performed the yeast experiments. Y. H. provided technical support on animal experiments. Y.Y. made the antibodies for HEV proteins. Q.D. contributed to the ORF3 mutant plasmids. Z.H., J.L. and L. F. performed the ion channel assays. M.T provided the yeast prion identification system. Y.N., H.C., Y.W., H. T. and M.T. analyzed the data and wrote the manuscript.

Competing interests: None.

Data availability statement: The authors confirm that all data supporting the findings are included in the article and SI Appendix.

Reference

1. Nagashima S, *et al.* (2017) Characterization of the Quasi-Enveloped Hepatitis E Virus Particles Released by the Cellular Exosomal Pathway. *Journal of Virology* 91(22).

2. Nan Y, Wu C, Zhao Q, & Zhou E-M (2017) Zoonotic Hepatitis E Virus: An Ignored Risk for Public Health. *Frontiers in microbiology* 8:2396.

3. Meng X-J (2013) Zoonotic and Foodborne Transmission of Hepatitis E Virus. *Seminars in liver disease* 33(01):041-049.

4. Dalton HR, *et al.* (2015) Hepatitis E virus and neurological injury. *Nature Reviews Neurology* 12(2):77-85.

5. Nair VP, *et al.* (2016) Endoplasmic Reticulum Stress Induced Synthesis of a Novel Viral Factor Mediates Efficient Replication of Genotype-1 Hepatitis E Virus. *PLoS Pathog* 12(4):e1005521.

6. Koonin EV, *et al.* (1992) Computer-assisted assignment of functional domains in the nonstructural polyprotein of hepatitis E virus: delineation of an additional group of positive-strand RNA plant and animal viruses. *Proceedings of the National Academy of Sciences* 89(17):8259-8263.

7. Graff J, Torian U, Nguyen H, & Emerson SU (2006) A Bicistronic Subgenomic mRNA Encodes both the ORF2 and ORF3 Proteins of Hepatitis E Virus. *Journal of Virology* 80(12):5919-5926.

8. Ding Q, *et al.* (2017) Hepatitis E virus ORF3 is a functional ion channel required for release of infectious particles. *Proc Natl Acad Sci U S A* 114(5):1147-1152.

9. Huang YW, Opriessnig T, Halbur PG, & Meng XJ (2007) Initiation at the third in-frame

AUG codon of open reading frame 3 of the hepatitis E virus is essential for viral infectivity in vivo. *J Virol* 81(6):3018-3026.

10. Kannan H, Fan S, Patel D, Bossis I, & Zhang YJ (2009) The hepatitis E virus open reading frame 3 product interacts with microtubules and interferes with their dynamics. *J Virol* 83(13):6375-6382.

11. Holla RP, Ahmad I, Ahmad Z, & Jameel S (2013) Molecular Virology of Hepatitis E Virus. *Seminars in Liver Disease* 33(1):3-14.

12. Zafrullah M, Ozdener MH, Panda SK, & Jameel S (1997) The ORF3 protein of hepatitis E virus is a phosphoprotein that associates with the cytoskeleton. *J Virol* 71(12):9045-9053.

13. Yamada K*, et al.* (2009) ORF3 protein of hepatitis E virus is essential for virion release from infected cells. *J Gen Virol* 90(Pt 8):1880-1891.

14. Nagashima S*, et al.* (2011) Tumour susceptibility gene 101 and the vacuolar protein sorting pathway are required for the release of hepatitis E virions. *J Gen Virol* 92(Pt 12):2838-2848.

15. Nan H, Chen H, Tuite MF, & Xu X (2019) A viral expression factor behaves as a prion. *Nature communications* 10(1):359.

16. Chakrabortee S*, et al.* (2016) Luminidependens (LD) is an Arabidopsis protein with prion behavior. *Proc Natl Acad Sci U S A* 113(21):6065-6070.

17. Yuan AH & Hochschild A (2017) A bacterial global regulator forms a prion. *Science* 355(6321):198-201.

18. Liu X*, et al.* (2025) Palmitoylation-dependent association with Annexin II directs

hepatitis E virus ORF3 sorting into vesicles and quasi-enveloped virions. *Proc Natl Acad Sci U S A* 122(1):e2418751122.

19. Halfmann R & Lindquist S (2008) Screening for amyloid aggregation by Semi-Denaturing Detergent-Agarose Gel Electrophoresis. *Journal of visualized experiments : JoVE* (17).

20. Jagusiak A*, et al.* (2019) Amyloids, Congo red and the apple-green effect. *Acta biochimica Polonica* 66(1):39-46.

21. Hou F*, et al.* (2011) MAVS forms functional prion-like aggregates to activate and propagate antiviral innate immune response. *Cell* 146(3):448-461.

22. Alberti S, Halfmann R, King O, Kapila A, & Lindquist S (2009) A systematic survey identifies prions and illuminates sequence features of prionogenic proteins. *Cell* 137(1):146-158.

23. Chernoff YO, Lindquist SL, Ono B, Inge-Vechtomov SG, & Liebman SW (1995) Role of the chaperone protein Hsp104 in propagation of the yeast prion-like factor [psi+]. *Science* 268(5212):880-884.

24. Jung G & Masison DC (2001) Guanidine hydrochloride inhibits Hsp104 activity in vivo: a possible explanation for its effect in curing yeast prions. *Current microbiology* 43(1):7-10.

25. Kushnirov VV, Dergalev AA, Alieva MK, & Alexandrov AI (2022) Structural Bases of Prion Variation in Yeast. *Int J Mol Sci* 23(10).

26. Lancaster AK, Nutter-Upham A, Lindquist S, & King OD (2014) PLAAC: a web and command-line application to identify proteins with prion-like amino acid composition.

Bioinformatics 30(17):2501-2502.

27. Yin X*, et al.* (2018) Origin, antigenicity, and function of a secreted form of ORF2 in hepatitis E virus infection. *Proceedings of the National Academy of Sciences* 115(18):4773-4778.

28. Nagashima S*, et al.* (2014) The membrane on the surface of hepatitis E virus particles is derived from the intracellular membrane and contains trans-Golgi network protein 2. *Arch Virol* 159(5):979-991.

29. Feng Z, Hirai-Yuki A, McKnight KL, & Lemon SM (2014) Naked Viruses That Aren't Always Naked: Quasi-Enveloped Agents of Acute Hepatitis. *Annual review of virology* 1(1):539-560.

30. Gouttenoire J*, et al.* (2018) Palmitoylation mediates membrane association of hepatitis E virus ORF3 protein and is required for infectious particle secretion. *PLoS Pathog* 14(12):e1007471.

31. Brigidi GS & Bamji SX (2013) Detection of protein palmitoylation in cultured hippocampal neurons by immunoprecipitation and acyl-biotin exchange (ABE). *Journal of visualized experiments : JoVE* (72).

32. Husain M & Harrod KS (2011) Enhanced acetylation of alpha-tubulin in influenza A virus infected epithelial cells. *FEBS Lett* 585(1):128-132.

33. Kapoor S, Srivastava S, & Panda D (2018) Indibulin dampens microtubule dynamics and produces synergistic antiproliferative effect with vinblastine in MCF-7 cells: Implications in cancer chemotherapy. *Scientific reports* 8(1):12363.

34. Tyagi S, Korkaya H, Zafrullah M, Jameel S, & Lal SK (2002) The phosphorylated form

of the ORF3 protein of hepatitis E virus interacts with its non-glycosylated form of the major capsid protein, ORF2. *J Biol Chem* 277(25):22759-22767.

35. Montpellier C*, et al.* (2018) Hepatitis E Virus Lifecycle and Identification of 3 Forms of the ORF2 Capsid Protein. *Gastroenterology* 154(1):211-223.e218.

36. Xu LD*, et al.* (2022) Revisiting the Mongolian Gerbil Model for Hepatitis E Virus by Reverse Genetics. *Microbiology spectrum* 10(2):e0219321.

37. Yakupova EI, Bobyleva LG, Vikhlyantsev IM, & Bobylev AG (2019) Congo Red and amyloids: history and relationship. *Bioscience reports* 39(1).

38. Lee AYS, Bayly A, & Lin MW (2021) Evaluation of Polarized Light and Fluorescence Microscopy of Congo Red Stain in the Diagnosis of Renal Amyloidosis. *Laboratory medicine* 52(6):574-577.

39. Sopova JV*, et al.* (2019) RNA-binding protein FXR1 is presented in rat brain in amyloid form. *Scientific reports* 9(1):18983.

40. Howie AJ & Owen-Casey MP (2010) Discrepancies between descriptions and illustrations of colours in Congo red-stained amyloid, and explanation of discrepant colours. *Amyloid : the international journal of experimental and clinical investigation : the official journal of the International Society of Amyloidosis* 17(3-4):109-117.

41. Bolton DC, McKinley MP, & Prusiner SB (1982) Identification of a protein that purifies with the scrapie prion. *Science* 218(4579):1309-1311.

42. Scheckel C & Aguzzi A (2018) Prions, prionoids and protein misfolding disorders. *Nature reviews. Genetics* 19(7):405-418.

43. Patel BK, Gavin-Smyth J, & Liebman SW (2009) The yeast global transcriptional

co-repressor protein Cyc8 can propagate as a prion. *Nat Cell Biol* 11(3):344-349.

44. Shahnawaz M, Park KW, Mukherjee A, Diaz-Espinoza R, & Soto C (2017) Prion-like characteristics of the bacterial protein Microcin E492. *Scientific reports* 7:45720.

45. Tetz G & Tetz V (2017) Prion-Like Domains in Phagobiota. *Frontiers in microbiology* 8:2239.

46. Tetz G & Tetz V (2018) Prion-like Domains in Eukaryotic Viruses. *Scientific reports* 8(1):8931.

47. Dennis EM & Garcia DM (2022) Biochemical Principles in Prion-Based Inheritance. *Epigenomes* 6(1).

48. Majumdar A*, et al.* (2012) Critical role of amyloid-like oligomers of Drosophila Orb2 in the persistence of memory. *Cell* 148(3):515-529.

49. Chapman MR*, et al.* (2002) Role of Escherichia coli curli operons in directing amyloid fiber formation. *Science* 295(5556):851-855.

50. Ramsook CB*, et al.* (2010) Yeast cell adhesion molecules have functional amyloid-forming sequences. *Eukaryot Cell* 9(3):393-404.

51. Geada MM, Galindo I, Lorenzo MM, Perdiguero B, & Blasco R (2001) Movements of vaccinia virus intracellular enveloped virions with GFP tagged to the F13L envelope protein. *J Gen Virol* 82(Pt 11):2747-2760.

52. Jouvenet N, Monaghan P, Way M, & Wileman T (2004) Transport of African swine fever virus from assembly sites to the plasma membrane is dependent on microtubules and conventional kinesin. *J Virol* 78(15):7990-8001.

53. Nishi M*, et al.* (2009) Requirement for microtubule integrity in the SOCS1-mediated

intracellular dynamics of HIV-1 Gag. *FEBS Lett* 583(8):1243-1250.

54. Leblanc JJ, Perez O, & Hope TJ (2008) Probing the structural states of human immunodeficiency virus type 1 pr55gag by using monoclonal antibodies. *J Virol* 82(5):2570-2574.

55. Naghavi MH & Walsh D (2017) Microtubule Regulation and Function during Virus Infection. *J Virol* 91(16).

56. Amorim MJ*, et al.* (2011) A Rab11- and microtubule-dependent mechanism for cytoplasmic transport of influenza A virus viral RNA. *J Virol* 85(9):4143-4156.

57. Yacovone SK*, et al.* (2016) Migration of Nucleocapsids in Vesicular Stomatitis Virus-Infected Cells Is Dependent on both Microtubules and Actin Filaments. *J Virol* 90(13):6159-6170.

58. Iwamoto M*, et al.* (2017) Functional association of cellular microtubules with viral capsid assembly supports efficient hepatitis B virus replication. *Scientific reports* 7(1):10620.

Fig. Legend

Fig. 1. HEV-ORF3 protein forms SDS-resistant high-molecular-weight aggregates in mammalian cells. A. SDS-PAGE and SDD-AGE analyses of HEV-ORF3 in S10-3 cells transfected with in vitro transcribed HEV-3 KernowC1-p6 or HEV-3 KernowC1-p6ΔORF3 RNA. The cells were harvested at 7 days post transfection using Laemmeli sample buffer for SDS-PAGE or the lysis buffer for SDD-AGE. After the separated proteins were transferred to PVDF membrane, ORF3 was detected with an HEV-3 ORF3 specific-monoclonal antibody (α-ORF3). The secreted ORF3 (Mono-ORF3) enriched from cell culture supernatant was included as ORF3 monomer control. HEV-ORF2 in the cell lysates was detected by rabbit anti-HEV-ORF2 polyclonal antibody (α-ORF2) as an infection control, and tubulin was probed as the protein loading control. **B.** SDS-PAGE and SDD-AGE analyses of HEV-ORF3 in infected HepG2/C3A cells. **C.** Observation of ORF3 fibril-like structure by TEM (left panel), and Congo Red Staining under a polarizing microscope (right panel). The ORF3 proteins were enriched from HEV-infected HepG2/C3A cells using immunoprecipitation method. **D.** Detection of the ORF3 fibril by TEM (left panel) and CR Staining (right panel). The ORF3 proteins were enriched from HEK-293T cells transfected with the plasmid expressing HEV-ORF3. **E.** HSP90 inhibitor suppressed ORF3 aggregates formation. HEK-293T cells were transfected with ORF3-expression plasmid for 6 hours, followed by treatment with 20 μM HSP90 inhibitor Geldanamycin (Geld). The inhibitor was replenished every 6 hours until 24 hours post-transfection. ORF3 was detected with an α-ORF3. **F.** Conversion of ORF3 monomer into aggregates *in vitro*. MYC-tagged ORF3 monomers were enriched from transfected HEK-293T cell culture supernatant, then incubated with the whole cell lysate of HEK-293T cell expressing untagged ORF3 for 30 min or 60 min at 37°C. The samples were subjected to SDS-PAGE and SDD-AGE analyses to examine the aggregation of MYC-tagged ORF3 monomer using monoclonal antibody against the MYC-tag (α-MYC).

Fig. 2. The HEV-ORF3 protein can functionally replace the prion-forming

domain of Sup35 in a yeast prion reporter assay. A. HEV-ORF3-Sup35MC confers inheritable [*ORF3*$^{+}$] and [*orf3*$^{-}$] phenotypes to yeast cells. Yeast *ade1-14* cells expressing HEV-ORF3-Sup35MC were spread on complete (1/4 YPD) medium. [*ORF3*$^{+}$] strains formed white colonies, which were distinguishable from [*orf3*$^{-}$] strains having red pigment accumulated through a block in the adenine biosynthetic pathway. Both phenotypes were stably inherited and the switch of [*ORF3*$^{+}$] and [*orf3*$^{-}$] phenotypes occurred at a low frequency during propagation (indicated by red arrows). Normal yeast *ade1-14* cells expressing wild-type Sup35 were included as controls to show the typical [*PSI*$^{+}$] and [*psi*$^{-}$] phenotypes. **B.** Detection of SDS-resistant aggregates in [*ORF3*$^{+}$] strains by SDD-AGE. The expression of HEV-ORF3-Sup35MC and Sup35 were probed by anti-Sup35 antibody (α-Sup35) in SDS-PAGE. The formation of SDS-resistant aggregates levels of HEV-ORF3-Sup35MC and Sup35 from corresponding phenotypes were examined by SDD-AGE and probed using a α-Sup35. **C.** The [*ORF3*$^{+}$] phenotype on 1/4 YPD medium is cured by the treatment with guanidine hydrochloride (GdnHCl). **D.** The [*ORF3*$^{+}$] phenotype on 1/4 YPD medium is curable by an *HSP104* gene knockout. **E.** The [*ORF3*$^{+}$] phenotype on medium lacking adenine (SD-Ade) is curable by *HSP104* gene knockout.

Fig. 3. Identification of the N terminal region of HEV-ORF3 as the candidate prion-forming domain (cPrD). A. Schematic illustration of ORF3 truncated mutants. **B.** SDS-PAGE and SDD-AGE analyses of overexpressed HEV-ORF3 truncated mutants. The truncated proteins were tagged with Venus protein and examined using anti-GFP polyclonal antibody (α-GFP). **C.** ORF3$_{T3}$-Sup35MC exhibits prion characteristics similar to Sup35 in yeast cells on 1/4 YPD and SD-Ade plates. ORF3$_{T4}$-Sup35MC and Sup35MC cells have a red phenotype on 1/4 YPD plate and impaired growth ability on SD-Ade medium. **D.** ORF3$_{T3}$-Sup35MC confers inheritable [*ORF3*$_{T3}$$^{+}$] and [*orf3*$_{t3}$$^{-}$] phenotypes to yeast cells. Red arrows indicate the switch of [*ORF3*$_{T3}$$^{+}$] and [*orf3*$_{t3}$$^{-}$] phenotypes. **E.** [*ORF3*$_{T3}$$^{+}$] and [*orf3*$_{t3}$$^{-}$] strains show distinguishable phenotypes on 1/4 YPD and SD-Ade plates. **F**. Formation of

aggregates in yeasts by ORF3 and its truncations. ORF3-GFP, $ORF3_{T1}$-GFP, and $ORF3_{T3}$-GFP produced bright foci (indicated by red arrows) in yeast cells. In contrast, $ORF3_{T2}$-GFP and $ORF3_{T4}$-GFP are evenly distributed. Scale bar, 5μm. **G.** Average number of aggregates per cell formed by different ORF3 truncations (T1 to T4). The florescence foci in the yeast cells were counted from three randomly selected images and then subjected to statistical analysis. All data are presented as mean ± SD and subjected to Student's *t*-test. *, $p < 0.05$; ****, $p < 0.0001$; ns, not significant. **H.** Detection of SDS-resistant aggregates of yeast strains expressing ORF3 truncated mutants by SDD-AGE. The yeast strains expressing the indicated mutants were harvested for SDD-AGE and probed by anti-Sup35 antibody (α-Sup35). The expression levels of the fusion proteins were examined by SDS-PAGE. The HEV-ORF3-Sup35MC expressing yeast was included as positive control.

Fig. 4. Phenylalanine at amino acid position 10 (F10) is a key residue for the prion-forming trait of ORF3. A. SDS-PAGE and SDD-AGE analyses of ORF3 triple alanine mutants. HEK-293T cells were respectively transfected with plasmids encoding wild type ORF3 (WT), the ORF3 mutants (M1 to M8) bearing triple alanine mutations in $ORF3_{T1}$, or Venus-$ORF3_{T2}$ (Venus-T2). The cells were harvested at 24 hours post transfection for SDS-PAGE (upper panel) or SDD-AGE (lower panel), and the truncated ORF3 proteins were probed using anti-ORF3 Mab (α-ORF3). Tubulin was probed as a protein loading control. **B.** Observation of the aggregation propensity of GFP tagged ORF3 triple alanine mutants in yeast cells by confocal microscopy. Red arrows indicate typical foci formed by the aggregated fluorescent proteins. Scale bar, 5μm. Average number of aggregates formed by different ORF3 mutants (M1 to M8) based on florescence foci in the yeast cells was counted from three randomly selected images and then subjected to statistics analysis. All data are presented as mean ± SD and subjected to Student's *t*-test. **, $p < 0.01$; ***, $p < 0.001$; ns, not significant. **C.** Phenotypic analysis of yeast cells bearing ORF3-Sup35MC triple alanine mutants on 1/4 YPD medium. **D.** Identification of $ORF3^{F10S}$ mutant with reduced ability to form SDS-resistant polymers. HEK-293T cells transfected with

plasmids encoding VN173-fused ORF3-WT and the indicated mutants were subjected to SDS-PAGE and SDD-AGE, detected using α-ORF3. **E.** ORF3^{F10S} mutant has reduced propensity to be converted into aggregates *in vitro*. The MYC tagged WT ORF3 or ORF3F10S monomer was enriched and incubated with the whole cell lysate (WCL) containing untagged WT ORF3 aggregates for 30 mins, then subjected to SDS-PAGE and SDD-ADE to examine the conversion of MYC tagged monomers into aggregates using an anti-MYC antibody (α-MYC). **F.** Phenotypic analysis of yeast cells bearing ORF3^{F10S}-Sup35MC on 1/4 YPD medium and SD-Ade medium. **G.** ORF3^{F10S}-Sup35MC showed reduced ability to form SDS-resistant polymers than ORF3-Sup35MC in yeast cells in SDD-AGE. The protein expression levels were examined by SDS-PAGE. ORF3-Sup35MC and ORF3^{F10S}-Sup35MC were probed by anti-Sup35 antibody (α-Sup35).

Fig. 5. Prion-like aggregation of the HEV-ORF3 protein is involved in HEV virion release from infected cells. A. Rescue of HEV-3 KernowC1-p6 ORF3^{F10S} mutant virus by reverse genetic system. S10-3 cells were transfected with the indicated viral RNAs and incubated for 7 days. HEV replication was determined by IFA using anti-ORF2 Mab-2G8 and anti-ORF3 polyclonal antibody. Scale bar, 100μm. **B.** Examination of the SDS-resistant aggregates formed by ORF3 and ORF3^{F10S} in HEV-RNA transfected S10-3 cells. The ORF3 proteins separated by SDS-PAGE (left panel) and SDD-AGE (right panel) were probed by anti-ORF3 Mab (α-ORF3). The expression of HEV capsid protein was detected using anti-ORF2 polyclonal antibody (α-ORF2) to indicate the accumulation of virus particles, and tubulin was probed to normalize protein loading. **C.** Quantification of the levels of positive-strand (+) and negative-strand (-) HEV-RNAs in transfected S10-3 cells by RT-qPCR. **D.** Quantification of the HEV RNA genome from cell culture supernatant by RT-qPCR. The cell culture supernatant of S10-3 cells was harvested at 2, 4 and 6 days post transfection of the indicated HEV-RNAs, then subjected to RT-qPCR analysis. **E.** Titration of the viruses released in the supernatant of S10-3 cells at 6 days post RNA transfection. The cell culture supernatant was harvested from S10-3 cells at 6 days

post transfection of the indicated HEV RNAs, and then used to infect fresh HepG2/C3A cells. HEV infection was determined by IFA using anti-ORF2 Mab-2G8 and observed under a fluorescence microscope. IFA positive cells were counted for quantification of infectious HEV particles. **F.** Quantification of the secreted ORF2 protein levels. Secreted form of HEV-ORF2 in the supernatant of S10-3 cells was quantified at 6 days post RNA transfection by ELISA using recombinant HEV-ORF2 as standard. **G.** Quantification of the secreted ORF3 protein levels by ELISA. Secreted form of HEV-ORF3 (sORF3) in the supernatant of S10-3 cells was captured by ORF3 specific Mab and detected using rabbit anti-ORF3 polyclonal antibody, followed by visualization using HRP-conjugated secondary antibody to determine the OD values. Experiments were repeated at least three times. All data are presented as mean ± SD and subjected to Student's t-test. **, $p < 0.01$; ****, $p < 0.0001$; ns, not significant.

Fig. 6. Prion-like aggregation of HEV-ORF3 stabilizes microtubule in HEV-permissive cells. A. F10S mutation interferes with the formation of filamentous structures by ORF3. S10-3 cells were transfected with plasmids expressing Venus-tagged HEV-3-ORF3 (WT) or F10S mutant (F10S) for 24 hours. The expression of the fluorescent ORF3 fusion protein (ORF2, Green channel) and the tubulin probed by an anti-tubulin antibody (Red channel) were observed under a confocal microscope. Scale bar, 10μm. Images shown here are representative of three independent biological replicates. **B.** The F10S mutation reduces the association of ORF3 with microtubules. S10-3 cells were transfected with plasmid expressing the indicated protein and subjected to microtubule isolation. The microtubule fraction (pellet) and cytoplasm fraction (supernatant) were examined by SDS-PAGE and immunoblotting using anti-acetylated-tubulin antibody (α-Ace-Tubulin) and anti-ORF3 Mab (α-ORF3). Total tubulin and GAPDH were probed to confirm the complete separation of microtubules and to normalize protein loading, respectively. Images shown here are representative of three independent biological replicates. **C.** The F10S mutation impairs the resistance to the microtubule assembly inhibitor

Indibulin confered by ORF3. S10-3 cells transfected with plasmids encoding WT-ORF3, F10S mutant or empty vector (EV) were subjected to the treatment of 1μM Indibulin to induce microtubule disassembly, and then analyzed by immunoblotting using α-Ace-Tubulin and α-ORF3. Total tubulin was probed to normalize the protein load. S10-3 cells treated with or without paclitaxel (Taxol) before Indibulin treatment were included as controls. Images shown here are representative of three independent biological replicates. **D.** Current–voltage relationship of *X. laevis* oocytes expressing WT-ORF3 and F10S mutant. During the current recording, the oocytes were bathed in Ringer solution. The voltage-clamp protocol employed rectangular voltage step pulses ranging from -90 mV to +60 mV in 10-mV increments. Each point represents the steady-state current at the corresponding voltage step. **E.** WT-ORF3 and F10S mutant expressed in *X. laevis* oocytes localize to the plasma membrane. The oocytes injected with the indicated mRNA were immunolabeled with α-ORF3 and analyzed by confocal microscopy. MOCK-treated oocyte was included as negative control. Scale bar, 70μm.

Fig. 7. Prion-like aggregation of HEV-ORF3 stabilizes microtubules in hepatocytes during HEV replication. A. The F10S mutation abolishes the role of ORF3 in enhancing tubulin acetylation. S10-3 cells were transfected with HEV-RNAs (KernowC1-p6 WT or KernowC1-p6 ORF3^{F10S}). Nocodazole treatment was carried out at a concentration of 20μM for 2 hours. Immunoblotting was performed using an anti-Ace-tubulin antibody (α-Ace-Tubulin), anti-ORF3-Mab (α-ORF3) and anti-HEV-ORF2-p239 polyclonal antibody (α-ORF2). Total tubulin was probed to normalize the protein load. **B.** Quantification analysis of tubulin acetylation level for S10-3 cell transfected HEV-RNAs from three independent biological replicates. ***, $p < 0.001$. ns, not significant. **C.** Nocodazole treatment suppressed HEV virion release. WT HEV-RNA transfected S10-3 cells were treated with the indicated doses of Nocodazole at 8-hour intervals for 3 days. Then cell culture supernatants were harvested for RT-qPCR to examine the release of HEV genome. All data are presented as mean ± SD (n=3) and subjected to Student's *t*-test. *, $p < 0.05$. **D.** Nocodazole

871 treatment resulted in the accumulation of HEV capsid protein ORF2 in infected cells.
872 S10-3 cells stably infected by HEV (KernowC1-p6 WT) were treated with the
873 indicated doses of Nocodazole at 8-hour intervals for 3 days. Immunoblotting was
874 performed using α-ORF2 to examine the intracellular accumulation of ORF2. Images
875 shown here are representative of three independent biological replicates. **E**. The F10S
876 mutation reduced the association of ORF3 with microtubules and impaired ORF2's
877 translocation to microtubules. S10-3 cells transfected with the indicated HEV-RNAs
878 were subjected to microtubule isolation. The microtubule fraction (pellet) and
879 cytoplasm fraction (supernatant) were examined by SDS-PAGE and immunoblotting
880 using α-Ace-Tubulin, α-ORF3 and α-ORF2. Total tubulin and GAPDH were probed
881 to confirm the complete separation of microtubules and to normalize protein loading,
882 respectively. Images shown here are representative of three independent biological
883 replicates.

884 **Fig. 8. Mutation of HEV-ORF3 cPrD reduces viral shedding and HEV-caused**
885 **hepatitis *in vivo*. A.** Quantification of viral RNA in the sera of HEV infected
886 Mongolian gerbils. The infectious clone was used for standard curve. **B**.
887 Quantification of viral RNA in the fecal samples of Mongolian gerbils. **C.** ELISA
888 Examination of anti-HEV IgG levels in the sera of Mongolian gerbils using
889 HEV-ORF2-p239 as the coating antigen. All data are presented as mean ± SD and
890 subjected to Student's *t*-test. *, $p < 0.05$; **, $p < 0.01$; ns, not significant. **D.**
891 Representative image for hematoxylin and eosin staining (left panel) and
892 immunohistochemistry staining (right panel) of liver section of infected Mongolian
893 gerbils at 14 dpi. HEV-ORF2 was probed by anti-ORF2 polyclonal antibody in
894 immunohistochemistry staining. **E.** Quantification of pathological changes of liver
895 sections. The liver sections of gerbils from different groups (n=5) were harvested at
896 42 dpi and assessed using Ishak scoring for histological grading. All data are
897 presented as mean ± SD and subjected to Student's *t*-test.

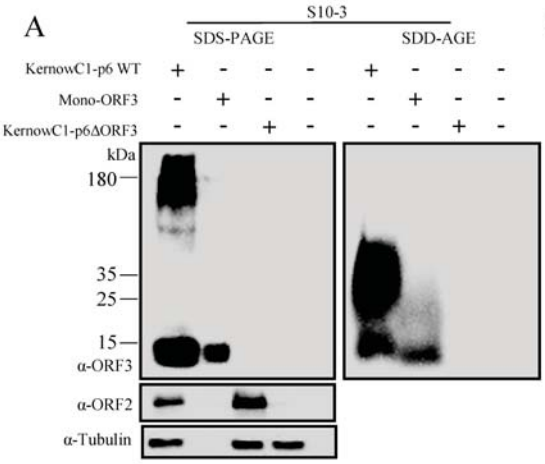
A
S10-3
SDS-PAGE
SDD-AGE
KernowC1-p6 WT
Mono-ORF3
KernowC1-p6ΔORF3
kDa
180
35
25
15
α-ORF3
α-ORF2
α-Tubulin

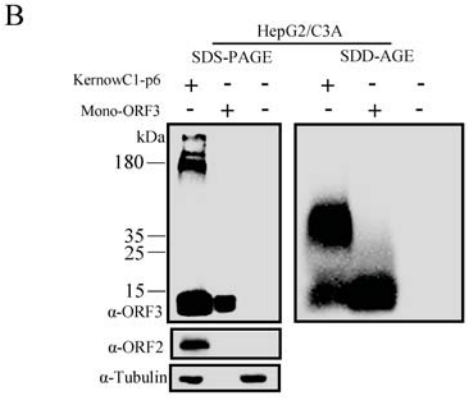
B
HepG2/C3A
SDS-PAGE
SDD-AGE
KernowC1-p6
Mono-ORF3
kDa
180
35
25
15
α-ORF3
α-ORF2
α-Tubulin

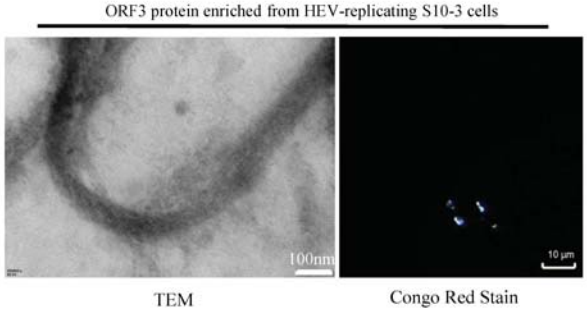
C
ORF3 protein enriched from HEV-replicating S10-3 cells
100nm
10 μm
TEM
Congo Red Stain

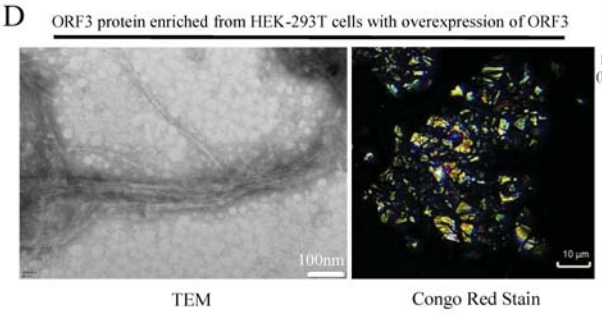
D
ORF3 protein enriched from HEK-293T cells with overexpression of ORF3
100nm
10 μm
TEM
Congo Red Stain

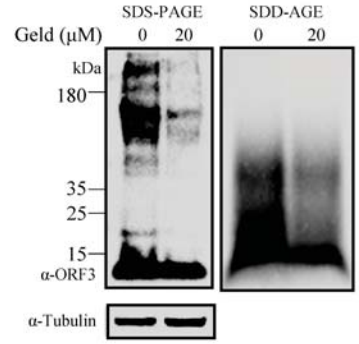
E
SDS-PAGE
SDD-AGE
Geld (μM)
0
20
0
20
kDa
180
35
25
15
α-ORF3
α-Tubulin

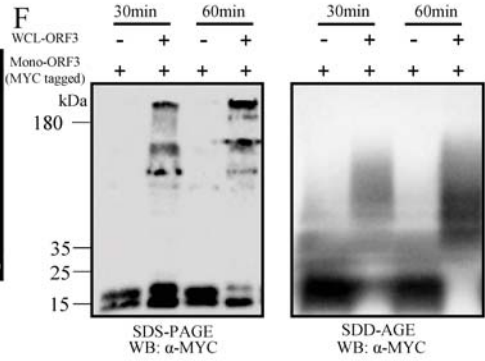
F
30min
60min
30min
60min
WCL-ORF3
Mono-ORF3
(MYC tagged)
kDa
180
35
25
15
SDS-PAGE
WB: α-MYC
SDD-AGE
WB: α-MYC

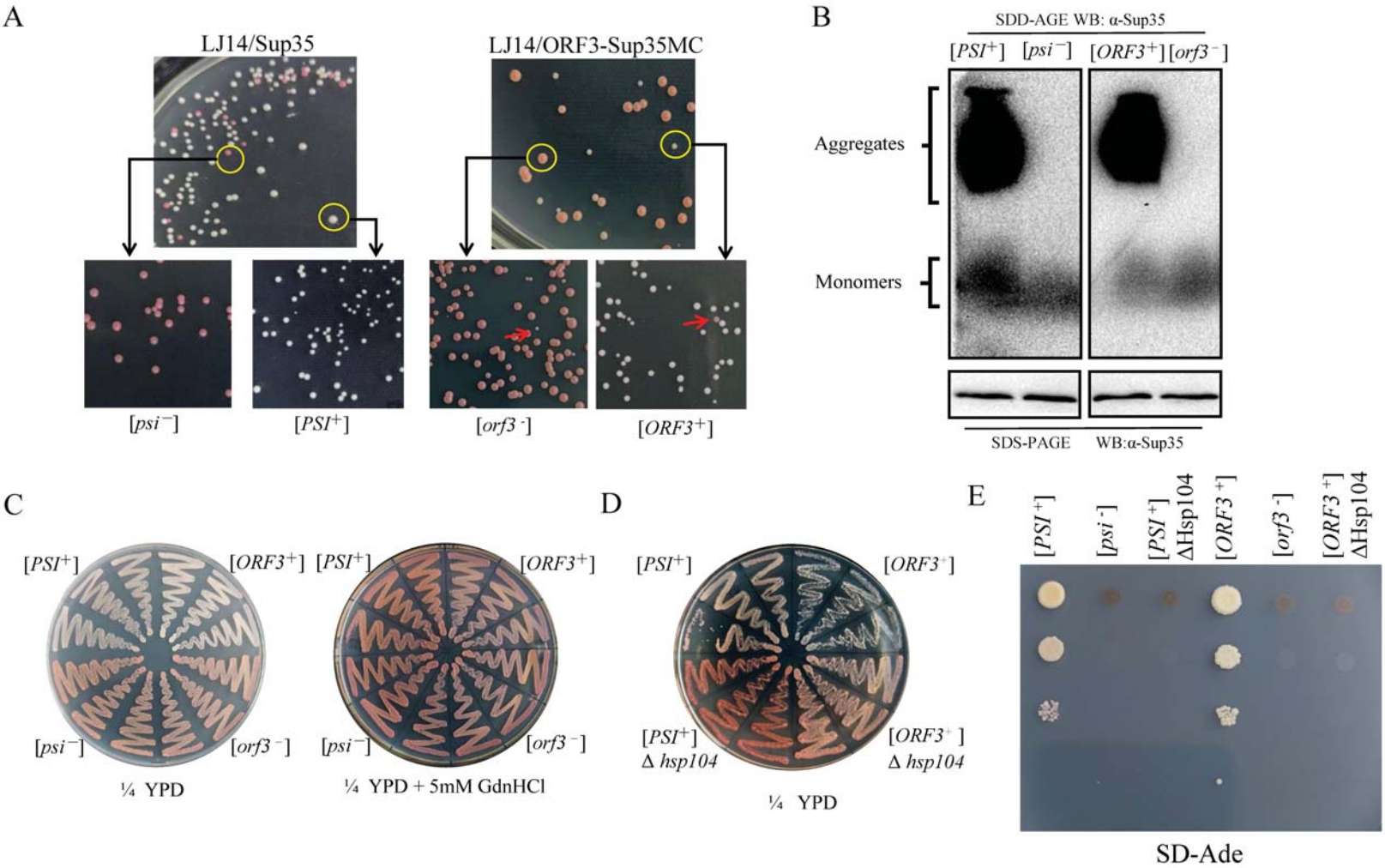
A
LJ14/Sup35
LJ14/ORF3-Sup35MC
[psi⁻]
[PSI⁺]
[orf3⁻]
[ORF3⁺]
B
SDD-AGE WB: α-Sup35
[PSI⁺] [psi⁻] [ORF3⁺] [orf3⁻]
Aggregates
Monomers
SDS-PAGE WB:α-Sup35
C
[PSI⁺] [ORF3⁺]
[psi⁻] [orf3⁻]
¼ YPD
[PSI⁺] [ORF3⁺]
[psi⁻] [orf3⁻]
¼ YPD + 5mM GdnHCl
D
[PSI⁺] [ORF3⁺]
[PSI⁺] Δ hsp104
[ORF3⁺] Δ hsp104
¼ YPD
E
[PSI⁺]
[psi⁻]
[PSI⁺] ΔHsp104
[ORF3⁺]
[orf3⁻]
[ORF3⁺] ΔHsp104
SD-Ade

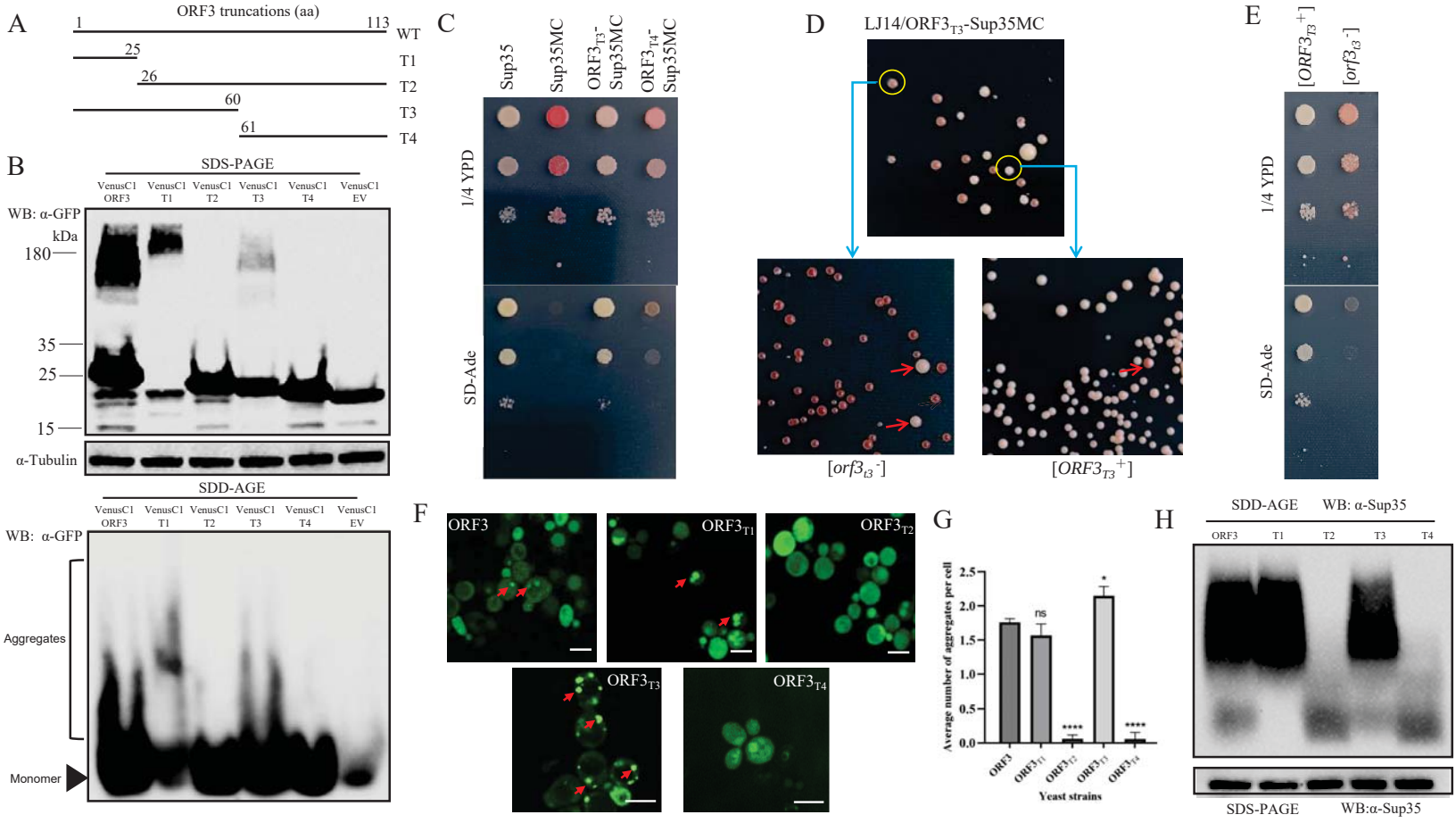
A
ORF3 truncations (aa)
1
113
WT
25
T1
26
T2
60
T3
61
T4
B
SDS-PAGE
VenusC1 ORF3
VenusC1 T1
VenusC1 T2
VenusC1 T3
VenusC1 T4
VenusC1 EV
WB: α-GFP
kDa
180
35
25
15
α-Tubulin
SDD-AGE
WB: α-GFP
Aggregates
Monomer
C
Sup35
Sup35MC
ORF3T3-Sup35MC
ORF3T4-Sup35MC
1/4 YPD
SD-Ade
D
LJ14/ORF3T3-Sup35MC
[orf3t3-]
[ORF3T3+]
E
[ORF3T3+]
[orf3t3-]
1/4 YPD
SD-Ade
F
ORF3
ORF3T1
ORF3T2
ORF3T3
ORF3T4
G
Average number of aggregates per cell
2.5
2.0
1.5
1.0
0.5
0.0
ns
*
****
****
ORF3
ORF3T1
ORF3T2
ORF3T3
ORF3T4
Yeast strains
H
SDD-AGE
WB: α-Sup35
ORF3
T1
T2
T3
T4
SDS-PAGE
WB:α-Sup35

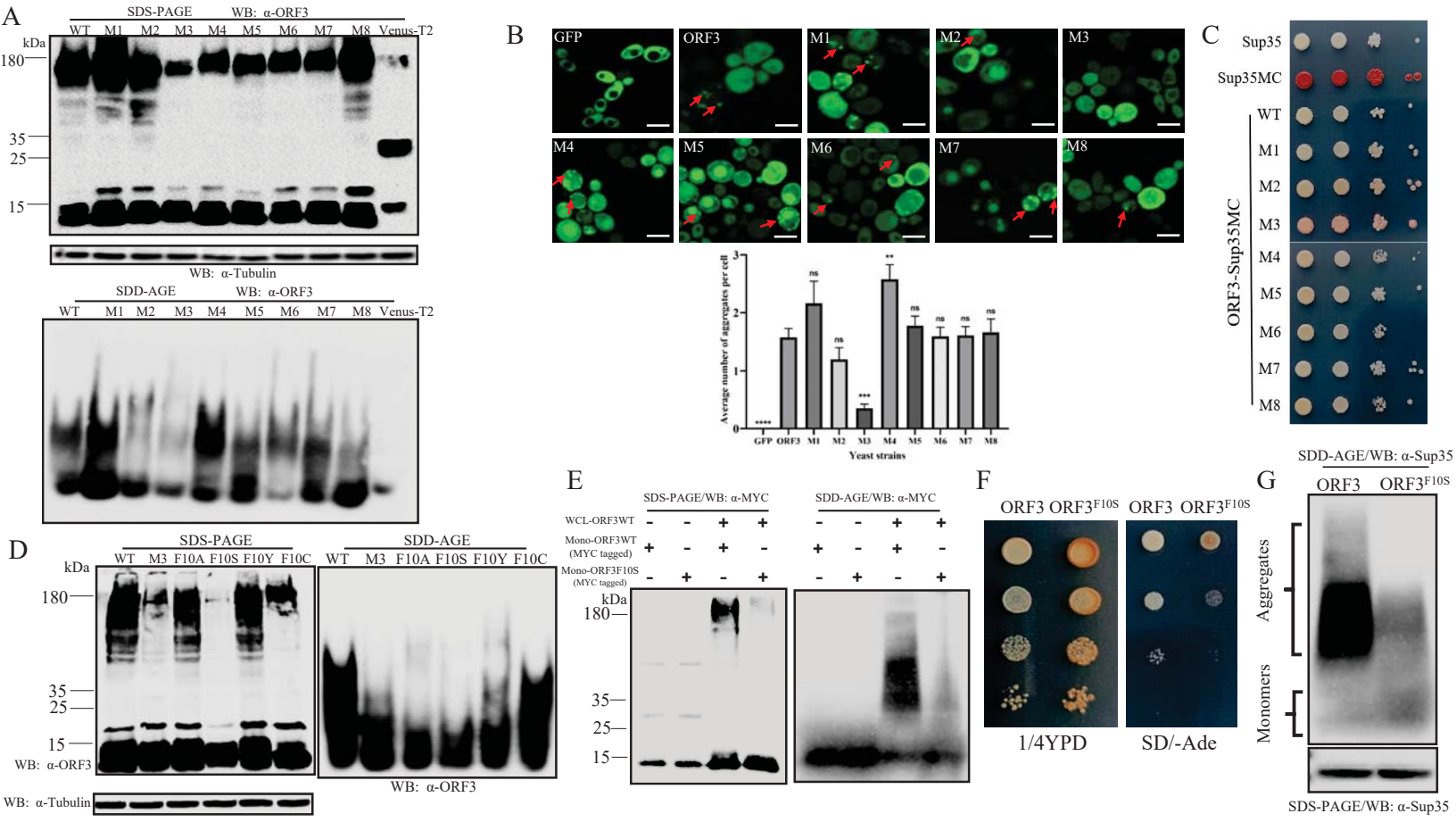
A
SDS-PAGE
WB: α-ORF3
WT M1 M2 M3 M4 M5 M6 M7 M8 Venus-T2
kDa
180
35
25
15
WB: α-Tubulin
SDD-AGE
WB: α-ORF3
WT M1 M2 M3 M4 M5 M6 M7 M8 Venus-T2
B
GFP
ORF3
M1
M2
M3
M4
M5
M6
M7
M8
Average number of aggregates per cell
Yeast strains
C
Sup35
Sup35MC
ORF3-Sup35MC
WT
M1
M2
M3
M4
M5
M6
M7
M8
D
SDS-PAGE
SDD-AGE
WT M3 F10A F10S F10Y F10C
kDa
180
35
25
15
WB: α-ORF3
WB: α-Tubulin
E
SDS-PAGE/WB: α-MYC
SDD-AGE/WB: α-MYC
WCL-ORF3WT
Mono-ORF3WT (MYC tagged)
Mono-ORF3F10S (MYC tagged)
kDa
180
35
25
15
F
ORF3 ORF3F10S
ORF3 ORF3F10S
1/4YPD
SD/-Ade
G
SDD-AGE/WB: α-Sup35
ORF3 ORF3F10S
Aggregates
Monomers
SDS-PAGE/WB: α-Sup35

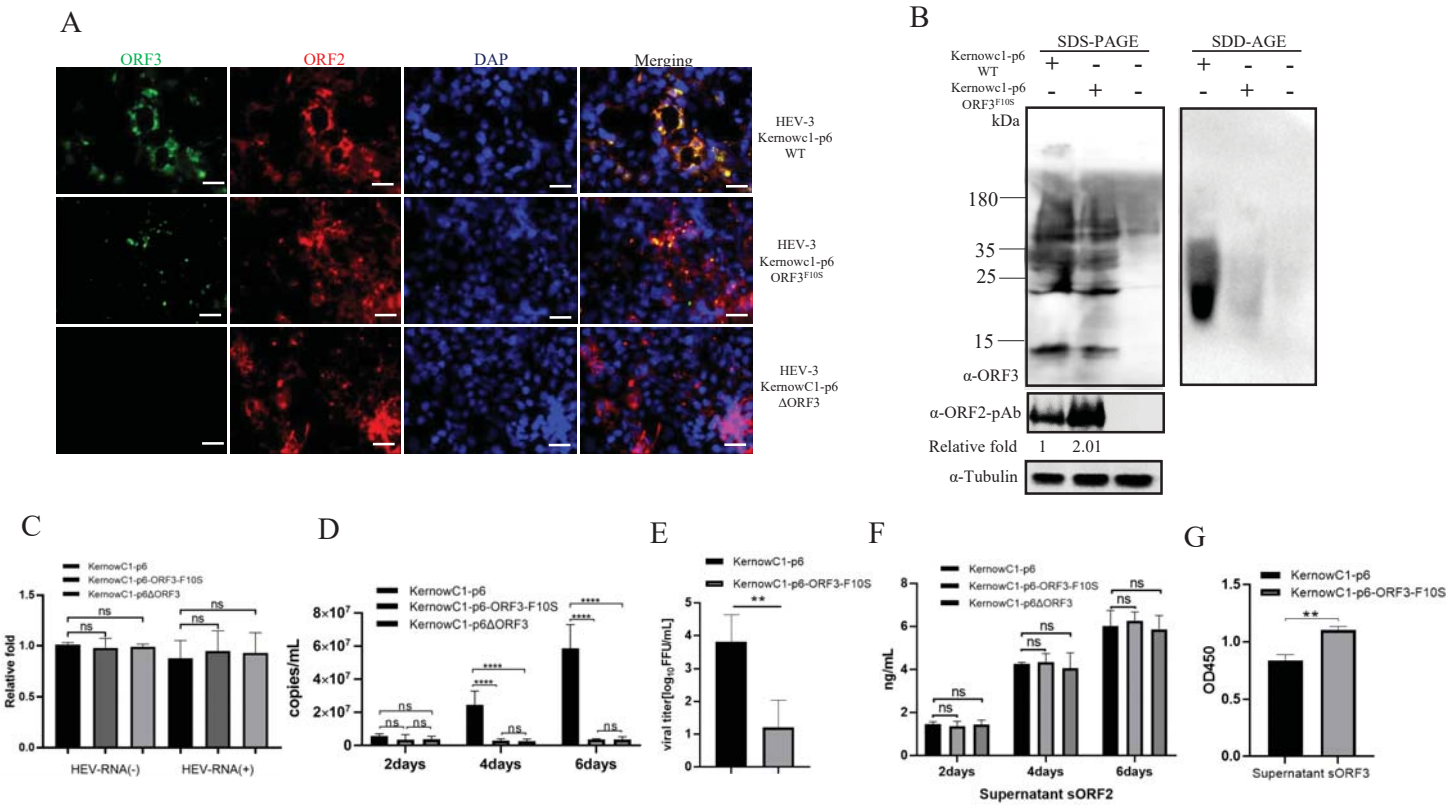
A
ORF3
ORF2
DAP
Merging
HEV-3 Kernowc1-p6 WT
HEV-3 Kernowc1-p6 ORF3F10S
HEV-3 KernowC1-p6 ΔORF3
B
SDS-PAGE
SDD-AGE
Kernowc1-p6 WT
Kernowc1-p6 ORF3F10S
kDa
180
35
25
15
α-ORF3
α-ORF2-pAb
Relative fold 1 2.01
α-Tubulin
C
KernowC1-p6
KernowC1-p6-ORF3-F10S
KernowC1-p6ΔORF3
Relative fold
HEV-RNA(-)
HEV-RNA(+)
D
copies/mL
2days
4days
6days
E
viral titer[log10FFU/mL]
F
ng/mL
Supernatant sORF2
G
OD450
Supernatant sORF3

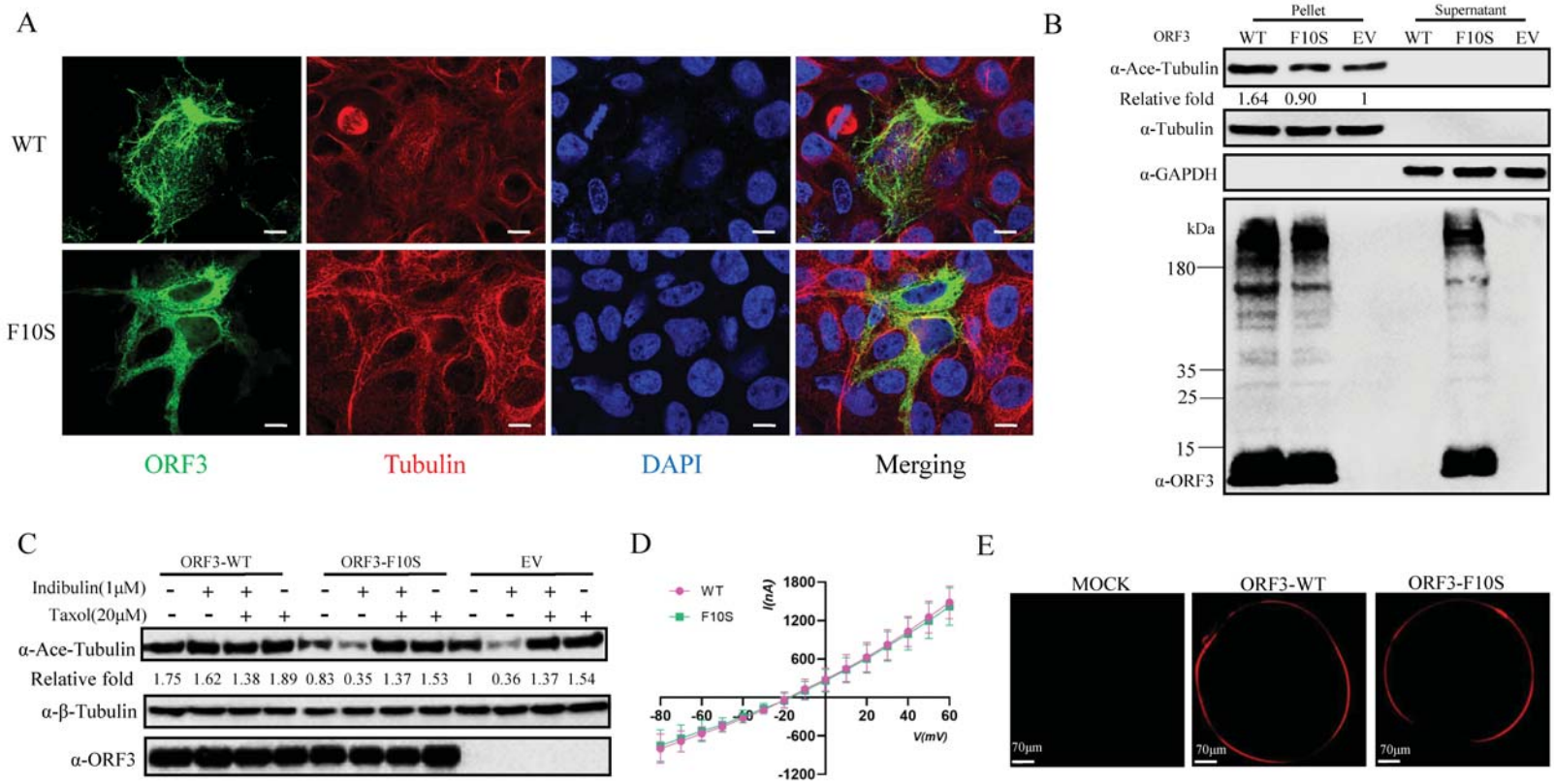
A
WT
F10S
ORF3
Tubulin
DAPI
Merging
B
Pellet
Supernatant
ORF3
WT F10S EV WT F10S EV
α-Ace-Tubulin
Relative fold 1.64 0.90 1
α-Tubulin
α-GAPDH
kDa
180
35
25
15
α-ORF3
C
ORF3-WT
ORF3-F10S
EV
Indibulin(1μM) - + + - - + + - - + + -
Taxol(20μM) - - + + - - + + - - + +
α-Ace-Tubulin
Relative fold 1.75 1.62 1.38 1.89 0.83 0.35 1.37 1.53 1 0.36 1.37 1.54
α-β-Tubulin
α-ORF3
D
WT
F10S
I(mA)
V(mV)
1800
1200
600
-600
-1200
-80 -60 -40 -20 20 40 60
E
MOCK
ORF3-WT
ORF3-F10S
70μm
70μm
70μm

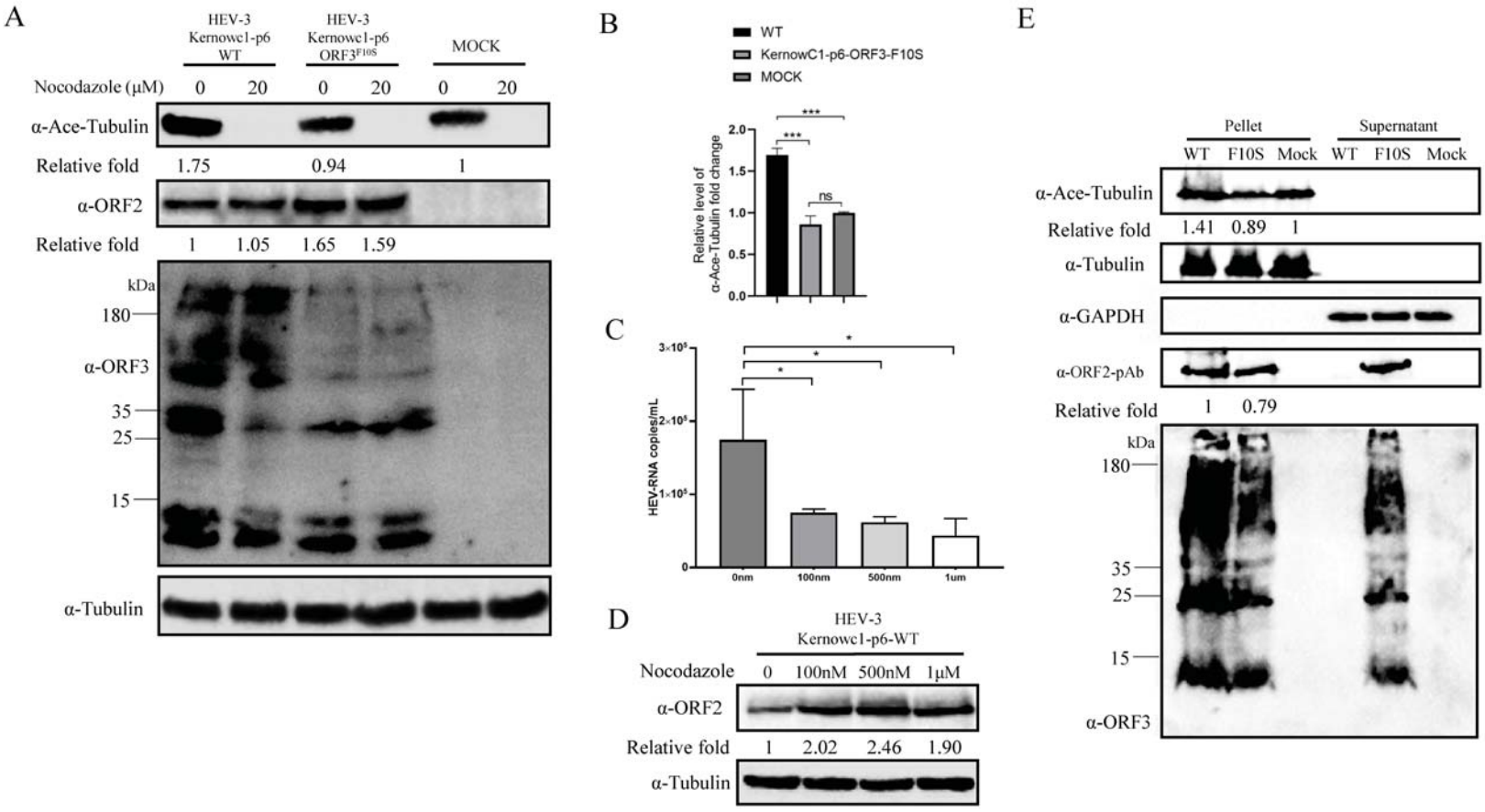
A
HEV-3 Kernowc1-p6 WT
HEV-3 Kernowc1-p6 ORF3F10S
MOCK
Nocodazole (μM) 0 20 0 20 0 20
α-Ace-Tubulin
Relative fold 1.75 0.94 1
α-ORF2
Relative fold 1 1.05 1.65 1.59
kDa
180
α-ORF3
35
25
15
α-Tubulin
B
WT
KernowC1-p6-ORF3-F10S
MOCK
Relative level of α-Ace-Tubulin fold change
***
***
ns
2.0
1.5
1.0
0.5
0.0
C
HEV-RNA copies/mL
3×10⁵
2×10⁵
1×10⁵
0
*
*
*
0nm
100nm
500nm
1um
D
HEV-3 Kernowc1-p6-WT
Nocodazole 0 100nM 500nM 1μM
α-ORF2
Relative fold 1 2.02 2.46 1.90
α-Tubulin
E
Pellet
Supernatant
WT F10S Mock WT F10S Mock
α-Ace-Tubulin
Relative fold 1.41 0.89 1
α-Tubulin
α-GAPDH
α-ORF2-pAb
Relative fold 1 0.79
kDa
180
35
25
15
α-ORF3

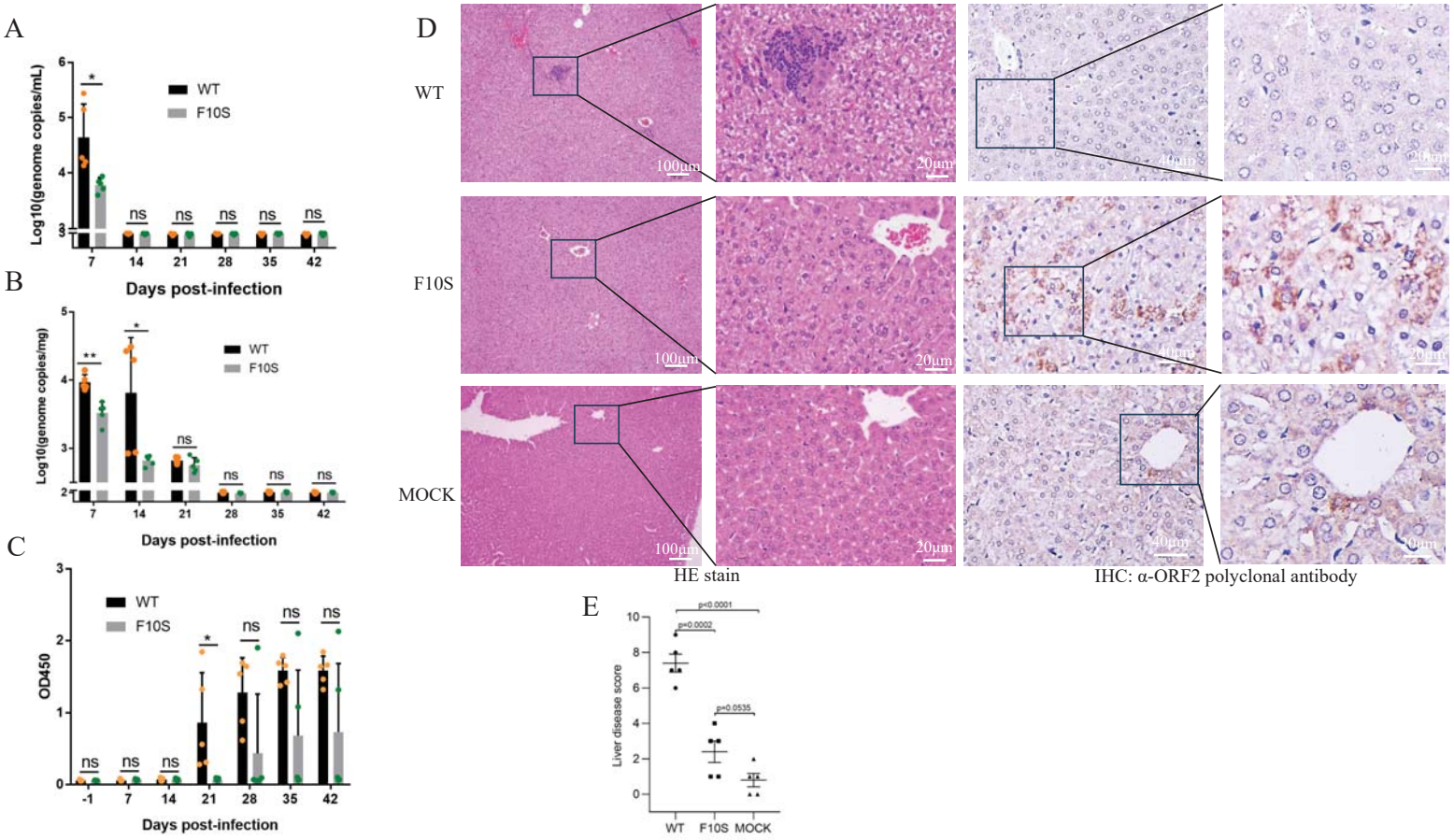
A
Log10(genome copies/mL)
WT
F10S
Days post-infection
B
Log10(genome copies/mg)
C
OD450
D
WT
F10S
MOCK
HE stain
IHC: α-ORF2 polyclonal antibody
E
Liver disease score
WT
F10S
MOCK